SMOS brightness temperature forward modelling and long term monitoring at ECMWF

Patricia de Rosnay, Joaquin Munoz-Sabater, Clément Albergel, Lars Isaksen, Stephen English, Matthias Drusch, Jean-Pierre Wigneron

Remote Sensing of Environment 237 (2020) 111424

Contents lists available at ScienceDirect

Remote Sensing of Environment

journal homepage: www.elsevier.com/locate/rse

SMOS brightness temperature forward modelling and long term monitoring at ECMWF

Patricia de Rosnay[a,*], Joaquín Muñoz-Sabater[a], Clément Albergel[a,1], Lars Isaksen[a], Stephen English[a], Matthias Drusch[b], Jean-Pierre Wigneron[c]

[a] European Centre for Medium-Range Weather Forecasts (ECMWF), Shinfield Park, RG2 9AX, Reading, UK
[b] European Space Agency, ESTEC, Noordwijk, the Netherlands
[c] Interactions Sol Plante Atmosphère (ISPA), Unité Mixte de Recherche 1391, Institut National de la Recherche Agronomique (INRA), CS 20032, 33882 Villenave d'Ornon CEDEX, France

ARTICLE INFO

Keywords:
SMOS
L-band
Forward modelling
CMEM
Bias correction
Reanalysis
Monitoring

ABSTRACT

This paper presents the forward modelling aspects of the SMOS (Soil Moisture and Ocean Salinity) activities at ECMWF (European Centre for Medium-Range Weather Forecasts). Several parameterizations of the Community Microwave Emission Modelling Platform (CMEM) are used to simulate L-band Brightness Temperatures (TBs) and compared to the SMOS TBs for 2010–2011. We show that simulated TBs are primarily sensitive, by order of importance, to the soil roughness model, the vegetation opacity and the soil dielectric model. In particular, best CMEM results are obtained with the simple Wigneron soil roughness model and the Wigneron model for the vegetation opacity. For the soil dielectric model, performances of the Wang and Schmugge and the Mironov models are shown to be similar and better than the Dobson model. The Wang and Schmugge model is then used in the next steps of this paper combined with the Wigneron roughness and vegetation models. The paper describes a multi-angular multi-polarised bias correction method based on a linear rescaling (mean and variance) computed at the monthly scale using SMOS observations and ECMWF-CMEM re-analysed TBs for a four year period (2010–2013). Results show that for 2010–2013 the seasonal multi-angular multi-polarisation bias correction approach reduces global RMSE to 7.91 K, compared to 16.7 K before bias correction, whereas the mean absolute bias is reduced to 1.39 K, compared to 11.04 K before bias correction. The consistency between the seasonality of simulated and the observed TBs is also improved by using a monthly bias correction, leading to correlation values improvement to 0.62 after bias correction compared to 0.56 before. The 2010–2013 bias correction applied to the 2014–2016 period at 40° incidence reduces the global RMSE from 15.56 K to 8.19 K, and the mean absolute bias from 10.16 K to 2.51 K, with no impact on the correlation values that remain at 0.61 in both cases. Long term monitoring of SMOS TB is presented covering a 7-year period (2010–2016) at both polarisations, at 40° incidence angle. Results show that the consistency between SMOS and ECMWF reanalysis-based TBs progressively improved between 2010 and 2016, pointing out improvements of level 1 SMOS TB products quality through the SMOS lifetime.

1. Introduction

Soil moisture is an important variable of the Earth System and it largely controls the water and energy budgets and the land-atmosphere interface (Taylor et al., 2012; Koster et al., 2004; Trenberth et al., 2007). Initial state of soil moisture influences weather prediction at the medium range (de Rosnay et al., 2013; Drusch, 2007) and at seasonal range (Koster et al., 2011). It is also of crucial importance for agricultural drought monitoring (Kumar et al., 2014) and flood forecasts (Wanders et al., 2014; Alfieri et al., 2013).

At continental and global scale land surface models (Balsamo et al., 2015; Reichle et al., 2011; Dirmeyer et al., 2006) and satellite sensors (Mecklenburg et al., 2016; Wagner et al., 2013; Entekhabi et al., 2010; Kerr et al., 2010b) provide reliable estimates of soil moisture. The Advanced Scatterometer (ASCAT) sensors on board the Metop satellite series have been providing active microwave C-Band (5.255 GHz) data since 2006. ASCAT surface soil moisture estimates are produced operationally, at resolutions of 50 km and 25 km, by EUMETSAT and made

* Corresponding author.
E-mail address: patricia.rosnay@ecmwf.int (P. de Rosnay).
[1] Present address CNRM, Université de Toulouse, Météo-France, CNRS, 31057 Toulouse, France.

https://doi.org/10.1016/j.rse.2019.111424
Received 14 February 2019; Received in revised form 5 September 2019; Accepted 13 September 2019
Available online 22 November 2019

available for Numerical Weather Prediction (NWP) Centres. Passive microwave at L-band (1.4 GHz) are highly sensitive to surface soil moisture and are used for soil moisture dedicated missions. It was first demonstrated with the Skylab mission which provided nine overpasses of L-band observations, at a resolution of 110 km, from 1973 to 1977 (Eagleman and Lin, 1976). The European Space Agency (ESA) Soil Moisture and Ocean Salinity (SMOS) mission was launched in 2009. SMOS was specifically designed for soil moisture measurements from space. Its concept relies on measurements of multi-angular fully polarised passive microwave emission of the Earth at L-band (1.4 GHz). SMOS Brightness Temperature (TB) observations have a resolution of about 40 km. These observations have been available in Near Real Time (NRT) since 2010. In 2016 a NRT level2 soil moisture product was developed based on a neural network soil moisture retrieval approach (Muñoz-Sabater et al., 2016; Rodríguez-Fernández et al., 2016, 2017). The NRT soil moisture product as well as the SMOS-IC product (Fernandez-Moran et al., 2017) are of great interest for operational hydrology applications in particular. Following SMOS, the National Aeronautics and Space Administration (NASA) Soil Moisture Active Passive (SMAP) mission (Entekhabi et al., 2010), was launched in January 2015. SMAP uses a rotating antenna, which takes measurements at a single incidence angle. The concept of SMAP is based on the combination of active and passive observations to produce high resolution (9 km) soil moisture estimates from Space. After the active sensor of SMAP failed in July 2015, it was decided the Sentinel-1 radar observations at C-band will be used for the active component of the SMAP mission (Das et al., 2018).

Several operational centres started to investigate the assimilation of L-band passive microwave observations from SMOS and SMAP in NWP systems, using either TB data, at ECMWF and Environnement and Climate Change Canada (ECCC), or using retrieved soil moisture products, e.g. at National Oceanic and Atmospheric Administration (NOAA) (Muñoz-Sabater et al., 2018, 2019; Carrera et al., 2017, 2015; Zhan et al., 2016). Furthermore, several studies were conducted to assimilate SMOS or SMAP TBs data in land surface models for soil moisture retrieval and/or processes studies (De Lannoy et al., 2013; De Lannoy and Reichle, 2015, 2016; Lievens et al., 2015). Using TBs data requires the use of a forward operator to simulate the TBs as seen from space. Different radiative transfer models are used in the community, which all rely on so-called tau-omega parameterisations such as those used in the SMOS and SMAP soil moisture retrieval (Kerr et al., 2010a; Reichle et al., 2016), or in the ECCC and ECMWF systems. The latter two systems use the Community Microwave Emission Modelling platform (CMEM) that was developed by ECMWF to simulate brightness temperatures at low frequency and based on state-of-the-art parameterisations (Holmes et al., 2008; de Rosnay et al., 2009a, b; Drusch et al., 2009; Muñoz-Sabater et al., 2011b; Albergel et al., 2012). At ECMWF the SMOS data is implemented in the Integrated Forecasting System (IFS) and used for SMOS monitoring (Muñoz-Sabater et al., 2011b). Drusch et al. (2009) conducted a first evaluation of the ECMWF forward simulation of L-band TBs against the historic Skylab observations (S-194 radiometer). Their study was preliminary; limited by the number of observations and the coarse resolutions of the observations and the ERA-40 reanalysis. However it allowed to show that the choice of parameterisations used in CMEM to account for vegetation opacity or soil roughness has a strong influence on the simulated TB. The authors showed that the simple parameterisation of Kirdyashev et al. (1979) for the vegetation opacity model provided TB in best agreement with the Skylab observations. de Rosnay et al. (2009a) used the Advanced Microwave Scanning Radiometer - Earth Observing System (AMSR-E) C-band TB observations over West Africa to evaluate CMEM for different combinations corresponding to 12 configurations of the soil dielectric model, soil roughness model and vegetation opacity model. More recently the capacity of the Variable Infiltration Capacity model coupled to CMEM was evaluated against SMOS L-Band observations over the upper Mississippi basin for 2010–2011 (Lievens et al., 2015).

This paper further investigates passive microwave forward modelling to use SMOS data for global NWP applications at ECMWF. Introducing a new observation type, such as SMOS measurements in this case, in a NWP system requires a number of technical and scientific developments. We first discuss the development and configuration of the CMEM observation operator, which is used to simulate measurements based on model output parameters. In this case, CMEM is applied to generate L-band TBs from a range of model fields, including soil temperature, soil moisture, vegetation type and properties. Some studies rely on calibration of the forward model parameters, as described for example by De Lannoy et al. (2013); De Lannoy and Reichle (2015). The approach used at ECMWF for SMOS is based on a bias correction that aims to minimise systematic differences between the simulated first guess TBs and the corresponding measurements. It relies on a linear rescaling approach as also used at ECCC (Carrera et al., 2015, 2017), but it accounts for combined multi-angular and seasonal corrections. The bias correction, which is used for data assimilation studies as presented in Muñoz-Sabater et al. (2018, 2019), is fully described in this paper and results are presented for sub-periods used to compute the parameters and for later years using independent observations. Finally, this paper presents long term SMOS TB monitoring results, based on ECMWF reanalysis-based forward brightness temperature, i.e. the simulated values and the measurements are compared over an extended multi-year period of time, to identify anomalies and trends in the data.

Section 2 presents the data and methods used in this paper. It describes the SMOS data, the ECMWF IFS and the CMEM forward operator. It also presents the microwave models inter-comparison methods and the multi-angular seasonal bias correction approach that was developed for SMOS. Section 3 presents results. It includes discussions on the results of the microwave models inter comparison results, the bias correction results and the 7-year SMOS monitoring statistics against the ERA-Interim based forward TB from ECMWF. Section 4 concludes.

2. Data and methods

2.1. SMOS brightness temperature observations

SMOS is a soil moisture remote sensing satellite mission (Kerr et al., 2010b, 2012; Mecklenburg et al., 2016). It provides 2D-interferometric measurements of multi-angular and full polarisation TBs at L-band (1.4 GHz) with a spatial resolution of 35 km to 50 km. At ECMWF the full operational Near Real Time (NRT) level 1 TB product of SMOS is used. It is available within 3 h of sensing, which is suitable for operational NWP applications. For this study we used the consistent reprocessed and operational level1 TB products from the SMOS processor v5.05 from January 2010 to March 2012 and from April 2012 to April 2015, respectively. Note that v5.05 is the latest reprocessed version available of the full NRT TB product. Therefore, from May 2015 to December 2016 the operational SMOS NRT TB from the processor version 6.20 was used.

TB data at X and Y polarisations at the antenna reference frame are used in this study. Observations at incidence angles of 30°, 40° and 50° were pre-processed by applying a noise filtering using a 2° binning angle, as described in Muñoz-Sabater et al. (2014). Quality control based on the NRT v5.05 product flag information was applied to ensure that only the Alias Free Field of View data is used for this study. We also discarded observations which are flagged to be affected by Radio Frequency Interferences (RFI), as well as observations with unrealistic TB values lower than 150 K or larger than 330 K. SMOS observations are discarded for pixels with fraction of water bodies larger than 5% or with radiometric accuracy exceeding 4 K.

The SMOS TB observations were interpolated, using a bi-linear interpolation approach, to the ECMWF reduced Gaussian model grid at 80 km resolution for the inter comparison study, and at 40 km for the bias correction and for the SMOS long term monitoring and comparison

with ERA-Interim based TBs for 2010–2016 (see Sections 2.4 for the experiments description).

2.2. ECMWF land surface model

H-TESSEL (Hydrology-Tiled ECMWF Scheme for Surface Exchanges over Land) is the land surface model used in the ECMWF IFS (Balsamo et al., 2015, 2009; van den Hurk et al., 2000; Viterbo and Beljaars, 1995). It is a point-wise land surface model, which represents the vertical soil water movements on each model grid-point by solving the Richard's equation (Richards, 1931) over four soil layers of 7 cm, 21 cm, 72 cm and 1.89 m thickness from top to bottom of the root zone. The surface runoff is based on the variable infiltration capacity (Balsamo et al., 2009). The soil texture is accounted for using the Food and Agriculture Organisation (FAO) Digital Soil Map of the World (DSMW) (FAO, 2003). H-TESSEL land use classification follows the Global Land Cover Characteristics (GLCC) data (Loveland et al., 2000), with assigned dominant high and low vegetation types. Land cover heterogeneities are represented using a tile approach that allows to account to a maximum of seven tiles per model grid point: bare soil, two tiles of vegetation (low and high), interception, two tiles for snow (exposed and shaded snow) and a lake tile as described in Dutra et al. (2010). The vegetation annual cycle is accounted for using a monthly Leaf Area Index climatology (Boussetta et al., 2013). Maps of lake fraction are derived at each model resolution using the GLOBCOVER land sea mask (http://due.esrin.esa.int/page_globcover.php) and a flood-filling algorithm (Documentation, 2018).

H-TESSEL is fully coupled to the atmosphere for NWP applications. It has also been used in stand-alone mode, forced by global reanalysis ERA-Interim atmospheric conditions available from 1979 (Dee et al., 2011) at a resolution of 80 km. The H-TESSEL soil moisture was evaluated against in situ soil moisture measurements by Albergel et al. (2013), showing good performance of the land surface model forced by ERA-Interim to capture soil moisture variabilities at time scales ranging from daily scale to seasonal and inter-annual scales.

In this paper, we use a global land-reanalysis produced by forcing H-TESSEL, cycle 41R1, by ERA-Interim atmospheric conditions. Using the offline land surface model may lead to some slight differences with the operational system used for data assimilation. However, it is necessary to use a consistent and recent version of the model through the SMOS lifetime rather than the operational system which relies on various versions of the system that included several resolution changes. Data assimilation results from Muñoz-Sabater et al. (2019) showed that bias correction parameters derived from this offline approach are reliable to use in the IFS. H-TESSEL simulations are conducted at a resolution of 40 km, which is the reduced Gaussian grid closest to the SMOS spatial resolution, for the period from 2010 to 2016, providing input land surface conditions, including soil moisture and temperature at different model depths, air temperature, and vegetation characteristics to CMEM.

2.3. The Community Microwave Emission Modelling Platform

CMEM is the forward operator used at ECMWF for low frequency passive microwave TB observations monitoring and data assimilation (de Rosnay et al., 2009a; Drusch et al., 2009; Holmes et al., 2008). It is a community model, developed and maintained by ECMWF. In this paper, the latest release of CMEM (v5.1) is described and the results presented in section 3.1 define the default configuration of this CMEM release that has been used for operational monitoring and research developments of SMOS TB data assimilation (Muñoz-Sabater et al., 2019). CMEM is an open source code, freely available to the scientific community from ECMWF, with an Apache licence. It has been used by a number of research and operational centres as forward model for low frequency passive microwave applications (Muñoz-Sabater et al., 2018; Carrera et al., 2015; Lievens et al., 2015).

For each model grid point, CMEM computes the Top-of-Atmosphere (TOA) TB $T_{Btoa,p,\theta}$ for each polarisation p (h or v for horizontal or vertical, respectively), and for each incidence angle θ. It is expressed as the sum of the ascending atmospheric emission ($T_{Bau,p}$) and the weighted sum of the $T_{Btov,p}(i)$, the TB computed at the top the vegetation for each individual land surface model tile (i = 1 to 7, see section 2.2 above):

$$T_{Btoa,p,\theta} = T_{Bau,p,\theta} + exp(-\tau_{atm,p,\theta}) \cdot \sum_{i=1}^{7} f(i) \cdot T_{Btov,p,\theta}(i) \quad (1)$$

where $\tau_{atm,p,\theta}$ is the atmospheric optical depth, and $f(i)$ is the fraction coverage of each tile.

Following state-of-the-art low frequency passive microwave modelling approaches such as described by Wigneron et al. (2017), assuming a single isothermal vegetation layer, the TB at the top of the vegetation layer computed for each tile as:

$$\begin{aligned} T_{Btov,p,\theta} &= (1 - r_{r,p,\theta}) \cdot T_{eff} \cdot exp(-\tau_{veg,p,\theta}) \\ &+ T_{Bveg,p,\theta}(1 + r_{r,p,\theta} \cdot exp(-\tau_{veg,p,\theta})) \\ &+ T_{Bad,p,\theta} \cdot r_{r,p,\theta} \cdot exp(-2 \cdot \tau_{veg,p,\theta}) \end{aligned} \quad (2)$$

where T_{eff} is the soil effective temperature, $r_{r,p,\theta}$ is the rough soil surface reflectivity (also expressed as one minus the emissivity $e_{r,p,\theta}$); $T_{BVeg,p,\theta}$ and $T_{Bad,p,\theta}$ are the TB of the vegetation and downward atmospheric components, respectively, and $\tau_{veg,p,\theta}$ is the vegetation optical depth at polarisation p and incidence angle θ.

CMEM is composed of four modules to compute the contributions from the soil, vegetation, snow and atmosphere to the TOA TB. It includes a choice of different parameterizations for each component of the modules as summarised in Table 1.

2.3.1. CMEM soil module

In the soil module, the dielectric mixing model is used to compute the soil dielectric constant depending on the microwave frequency, soil moisture and temperature and soil texture. Three parameterizations are implemented in CMEM to infer the soil dielectric constant. The Dobson model is valid for frequency in a range of 1 GHz to 20 GHz (Dobson et al., 1985). The Mironov (Mironov et al., 2004) and the Wang and Schmugge (1980) models are valid for frequencies between 1 GHz and 10 GHz. Results from de Rosnay et al. (2009a) over West Africa showed that the Wang and Schmugge model and the Mironov model perform better than the Dobson model at C-band. They account for the effect of bound soil water and they are more suitable for a large range of frequencies. The Mironov parameterisation has been widely used for L-band applications at the field scale (Mialon et al., 2012, for example), and at global scale in particular in the SMOS retrieval algorithm (Kerr et al., 2016).

The soil TB is expressed, following the Rayleigh-Jeans approximation, as the product between the effective temperature T_{eff} and the rough soil emissivity $e_{r,p,\theta}$. A simple model was proposed by Choudhury et al. (1982) to approximate the effective temperature as a function of the surface soil temperature (at ~5 cm), soil temperature at depth (at ~50 cm) and a frequency dependent parameter. This parameterisation was modified by Wigneron et al. (2001) for L-band radiometry to account for soil moisture in the parameter. Holmes et al. (2006) introduced further dependence to the soil conditions in the empirical parameter with the dielectric constant. Based on the long term SMOSREX data set, in southwest of France, de Rosnay et al. (2006) compared these parameterizations and showed that the Wigneron et al. (2001) was best suited for global scale studies. This parameterisation is used as default configuration in CMEM to compute the soil effective temperature (de Rosnay et al., 2009a).

Soil roughness has a large impact on soil emission and reflectivity (Mialon et al., 2012; Escorihuela et al., 2007). Increase in surface roughness leads to higher emissivities and reduced differences between horizontally and vertically polarized brightness temperatures. CMEM includes five soil roughness parameterizations (listed in Table 1), all derived from the semi-empirical approach proposed by Wang and

Table 1
Modular configuration of CMEM. For each module components, a choice of parameterizations is available. Parameterizations in bold are those used in this paper. Different combinations of CMEM using three different dielectric models, four roughness models and three vegetation optical depths models are compared, leading to 36 configurations evaluated against SMOS observations.

CMEM modules	Choice of parameterizations	
	Short name	Reference
Soil module:		
Dielectric mixing model	**Dobson**	(Dobson et al., 1985),
	Mironov	Mironov et al. (2004)
	Wang	Wang and Schmugge (1980)
Effective temperature model	Surface temperature forcing,	
	Choudhury	Choudhury et al. (1982)
	Wigneron	Wigneron et al. (2001)
	Holmes	Holmes et al. (2006)
Soil roughness model	**Choudhury**	(Choudhury et al., 1979),
	Wign07	Wigneron et al. (2007)
	Wign01	Wigneron et al. (2001)
	Texture dependent	citepatbd:10
	Wegmüller	Wegmüller and Mätzler (1999)
Vegetation module:		
Vegetation optical depth model	Wegmüller	(Wegmüller et al., 1995),
	Jackson	Jackson and O'Neill (1990)
	Kirdyashev	Kirdyashev et al. (1979)
	Wigneron	Wigneron et al. (2007)
Snow module:		
Snow emission model	HUT single layer model	Pulliainen et al. (1999)
Atmospheric module:		
Atmospheric emission model	**Pellarin**	(Pellarin et al., 2003),
	Ulaby	Ulaby et al. (1986)

Choudhury (1981) and described in detail in Muñoz-Sabater et al. (2011a). The rough soil reflectivity is computed as:

$$r_{r,p,\theta} = (Q \cdot r_{s,q,\theta} + (1 - Q) \cdot r_{s,p,\theta}) \cdot exp(-h \cdot cos^N \theta) \quad (3)$$

where $r_{s,q,\theta}$ is the the specular reflectivity (from the Fresnel equations), p and q are polarisations, and θ the incidence angle. The parameters Q, N and h account for polarisation mixing, angular dependence, and roughness. The value of Q is zero at L-band (Lawrence et al. (2013); Wigneron et al. (2007); Njoku et al. (2003)). Two parameterisations are derived from Equation (3), with $N = 0$ and:

$$h = (2k\sigma)^2 \ (Choudhury) \quad (4)$$

$$h = 1.3972 \cdot (\sigma / L_c)^{0.5879} \ (Wigneron\ 2001) \quad (5)$$

with k the wave number, L_c the correlation length and σ the surface roughness standard deviation. Soil roughness parameters cannot be measured accurately at global scale. They can be calibrated a priori, providing constant maps of roughness coefficients, to minimise climatological biases (De Lannoy et al., 2013). However calibration may compensate for simplified parameterisations in other components of the forward model and lead to unrealistic parameter values. Besides, calibrated coefficients do not capture temporal variations in roughness characteristics related to hydro-meteorological conditions or to crop management practices, for example. In this study soil roughness parameters used for the Choudhury and Wigneron (2001) models (Equations (4) and (5)) are set to a constant value in space and time (σ = 2.2 cm and L_c = 6 cm) following the approach of Carrera et al. (2015); Drusch et al. (2009); de Rosnay et al. (2009a), and using parameters as defined by Muñoz-Sabater et al. (2011a). We also use two soil roughness models for which parameter values are non constant over the globe as they account for soil moisture and soil texture (Kerr et al., 2010a), or for the vegetation type as described in Wigneron et al. (2007). For these parameterisations, CMEM relies on the H-TESSEL physiographic information (look-up tables) for soil texture and land cover (see Section 2.2). The Wegmüller and Mätzler (1999) model, which is included in CMEM and uses a single roughness parameter $h = k \cdot \sigma$, is not used in this study. Table 1 highlights in bold the CMEM parameterizations used and evaluated against the SMOS observations in this paper.

2.3.2. CMEM vegetation module

The vegetation layer is represented in CMEM following the $\tau - \omega$ approach. As formulated in Equation (2), vegetation contributes in several ways to the measured signal at the top of the atmosphere. It attenuates the soil emission, the downward atmospheric emission and the upward atmospheric emission after it was reflected on the soil surface, and it has a direct contribution to the signal expressed as:

$$T_{Bveg,p} = T_c \cdot (1 - \omega_p) \cdot (1 - exp(-\tau_{veg,p})) \quad (6)$$

where T_c is the canopy temperature and ω_p is the single scattering albedo at polarisation p. CMEM includes a choice of four parameterisations to account for the vegetation effect on the signal. They differ in the approach used to compute the vegetation optical depth depending on the Leaf Area Index and vegetation water content as described in details in a number of papers including for example (de Rosnay et al., 2009a; Drusch et al., 2009; Wigneron et al., 2007). In this paper we use the GLCC (Loveland et al., 2000) physiographic information for vegetation type and vegetation cover used in H-TESSEL with the seasonally varying Leaf Area Index from the climatology as described in Boussetta et al. (2013) (see section2.2).

While the parameterizations from Wigneron et al. (2007) and Jackson and O'Neill (1990) are most suitable at L-band, the Kirdyashev et al. (1979) and Wegmüller et al. (1995) models account for the wave number in their parameterisation of the optical depth. They are applicable for a larger range of frequencies. In this paper CMEM performances are compared and evaluated against SMOS data, for different

Table 2
Description of the numerical experiments conducted for model configuration, bias correction and long term evaluation and monitoring purposes. The 36 experiments of Set 1 use different CMEM configurations corresponding to different combinations of parameterisations shown in Table 1. Experiments conducted for Set 2 and Set 3 rely on the best CMEM configuration selected after Set 1 experiments are compared to SMOS data.

Purpose	Set	Number	Period	Resolution	Incidence	SMOS	Results
	name	of runs			angle	processor	
CMEM configuration	Set 1	36	2010–2011	80 km (TL255)	40°	v5	Section 3.1
Bias correction	Set 2	1	2010–2013	40 km (TL511)	30° , 40° , 50°	v5	Section 3.2
Long term evaluation and monitoring	Set 3	1	2010–2016	40 km (TL511)	40°	v5 (until 04.2015) v6 (from 05.2015)	Section 3.2,3.3

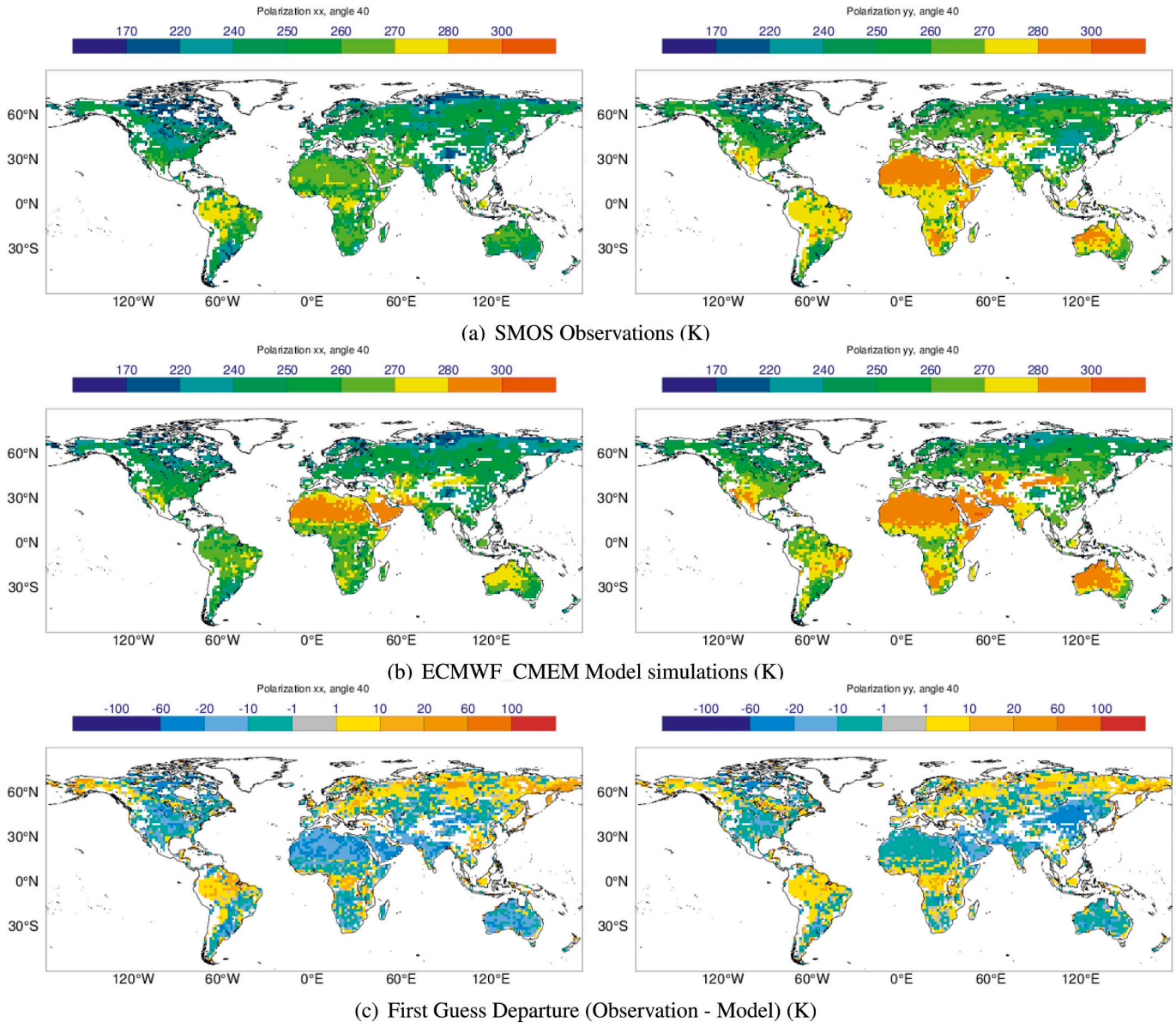

Figure 1. L-band TB (K) annual mean maps (2010–2011), at 40° incidence angle, X polarisation (left) and Y polarisation (right), observed by SMOS (a), simulated by ECMWF (b), and first guess departure (Observation-Model, c). ECMWF TBs shown here are obtained from one of the Set1 experiments (Table 2), using the dielectric model of Wang and Schmugge (1981), the simple soil roughness Model of Wigneron et al. (2001) and the Wigneron et al. (2007) vegetation opacity model.

configurations using the parameterizations of Wigneron et al. (2007), Jackson and O'Neill (1990), and Kirdyashev et al. (1979).

2.3.3. CMEM snow and atmospheric modules

In the case of presence of snow, CMEM accounts for a snow layer as described in Holmes et al. (2008) with the snow reflectivity computed using the single layer version of the Helsinki University of Technology (HUT) model (Pulliainen et al., 1999). In this study the snow covered areas are filtered out in the quality control as described in the next subsection.

In the atmospheric module of CMEM, the atmosphere optical thickness $\tau_{atm,p}$ is computed following the parameterisation developed by Pellarin et al. (2003).

2.3.4. Faraday rotation

CMEM as described above simulates TOA TB in the Earth reference frame at both horizontal and vertical polarisations. These TB need to be transformed into the SMOS antenna frame to be compared to the SMOS data. The transformation of CMEM's $T_{Btoa,h}$ and $T_{Btoa,v}$ into the SMOS antenna frame, as described in the Kerr et al. (2010a), accounts for the SMOS geometry and to the Faraday rotation in the ionosphere. The latter causes a rotation of the plane of polarisation and the strength of the rotation is proportional to the electronic content of the ionosphere. Generally speaking it produces a change of only a few K to the TOA TB. In dual polarisation mode, used for SMOS monitoring and assimilation activities over land surfaces, the transformation of TB is expressed as follows:

$$\begin{bmatrix} T_{Becm,X,\theta} \\ T_{Becm,Y,\theta} \end{bmatrix} = \begin{bmatrix} cos^2(a) & sin^2(a) \\ sin^2(a) & cos^2(a) \end{bmatrix} \begin{bmatrix} T_{Btoa,h,\theta} \\ T_{Btoa,v,\theta} \end{bmatrix} \quad (7)$$

where a is the total rotation angle computed as sum of the geometric and the faraday rotation angles. This transformation is included as a CMEM post-processing step in the ECMWF IFS. In the following of the paper, we use $T_{Becm,X,\theta}$ and $T_{Becm,Y,\theta}$ from CMEM to compare with the SMOS TB data in the antenna frame.

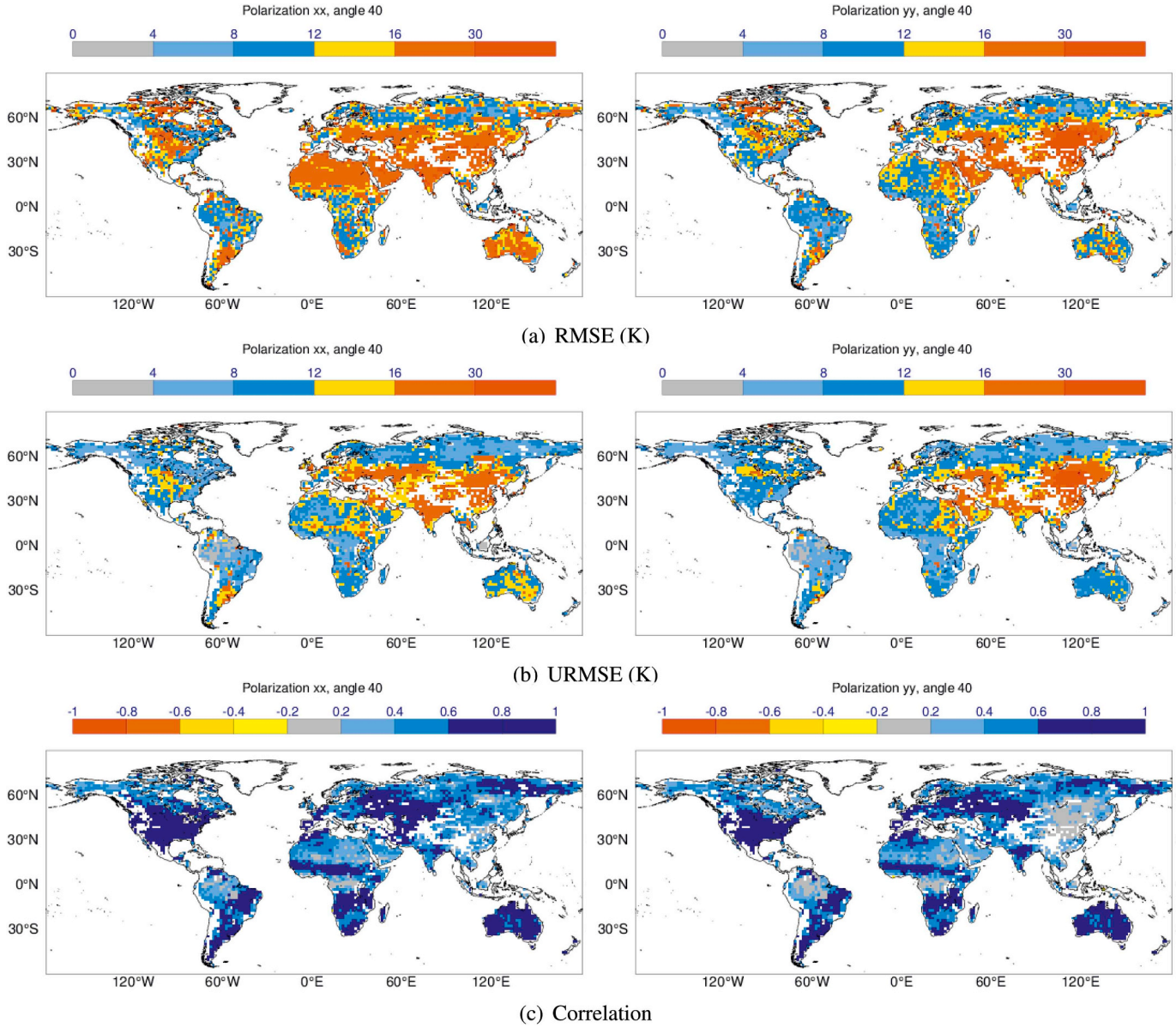

Figure 2. Comparison between SMOS observations and simulated L-band TB for 2010–2011, at 40° incidence angle, at X polarisation (left) and Y polarisation (right): RMSE (a), URMSE (b) and correlation (c). ECMWF TBs shown here are obtained from one of the Set1 experiments (Table 2), using the dielectric model of Wang and Schmugge, the simple soil roughness Model of Wigneron et al. (2001) and the Wigneron et al. (2007) vegetation opacity model.

2.4. Numerical experiments

A series of numerical experiments were conducted with CMEM, using the H-TESSEL land surface model input, to define CMEM's configuration, to develop and evaluate bias correction, and to assess long term SMOS monitoring statistics. To identify CMEM's bests configurations, 36 different CMEM configurations, corresponding to different combinations of three dielectric models, three vegetation opacity models and four roughness models presented in Table 1, were evaluated against SMOS TB observations. Due to the large number of experiments, this set was limited to 40° incidence angle and it was conducted at a resolution of 80 km for a two-year period (2010–2011). To develop the bias correction, the selected best CMEM configuration was used and numerical experiments were conducted at three different incidence angles, 30°, 40° and 50°, at a resolution of 40 km, which is close to the SMOS resolution, for 2010–2013. The 40° experiment was extended for 2014–2016 and used to evaluate the bias correction using independent data and for long term monitoring purpose. Table 2 summarises the experiments conducted. It also indicates the version of the SMOS processor used to produce the SMOS data compared to the ERA-Interim based CMEM forward TBs, and it indicates in which section the results are presented.

In addition to the quality control described in Section 2.1, which was based on the SMOS product quality flags, we used the reanalysed land surface conditions from H-TESSEL from each experiment to discard model and observation values for grid points with presence of snow, and grid points with air temperature lower than 273 K. We also discarded areas with complex topography with a slope larger than 4%, and areas with water fraction larger than 5%.

2.5. Bias correction method

At ECMWF, SMOS TBs are being processed and monitored for a continuous assessment of the quality of the measurements. For the analysis experiments, such as described in Muñoz-Sabater et al. (2018, 2019), they are used in the land surface analysis to initialise the NWP

Table 3
Statistics of the global scale comparison between ECMWF ERA-Interim-based CMEM simulations and SMOS observations of L-band brightness temperature at X polarisation for a 40° incidence angle for 2010–2011 for 36 CMEM configurations of Set 1 experiments (see Tables 1 and 2). For each dielectric model best statistics are highlighted in bold. SDV is the normalised standard deviation (ratio between the simulated and observed TB standard deviations).

Dielectric Model	Vegetation Opacity Model	Soil Roughness Model	R	uRMSE (K)	Bias (K)	SDV
Dobson	Jackson	Choudhury	0.53	12.00	−20.92	0.45
		Wign07	**0.56**	11.90	**−0.16**	0.71
		Wign01	**0.56**	11.77	−7.13	0.59
		Texture dependent	0.55	13.20	17.17	0.92
	Kirdyashev	Choudhury	0.54	11.90	−20.04	0.45
		Wign07	0.54	12.14	5.71	0.72
		Wign01	0.55	11.82	−2.30	0.58
		Texture dependent	0.46	14.28	29.10	**0.97**
	Wigneron	Choudhury	0.54	11.92	−19.06	0.46
		Wign07	**0.56**	11.96	5.09	0.76
		Wign01	**0.56**	**11.70**	−2.20	0.63
		Texture dependent	0.55	13.57	27.65	**1.03**
Mironov	Jackson	Choudhury	0.53	11.93	−21.98	0.45
		Wign07	**0.57**	11.81	−3.15	0.72
		Wign01	**0.57**	11.65	−9.69	0.60
		Texture dependent	0.56	13.21	12.01	0.94
	Kirdyashev	Choudhury	0.55	11.82	−21.29	0.46
		Wign07	0.54	12.17	2.18	0.75
		Wign01	0.55	11.76	−5.34	0.62
		Texture dependent	0.48	14.61	22.96	**1.05**
	Wigneron	Choudhury	0.55	11.84	−20.24	0.47
		Wign07	**0.57**	11.91	**1.76**	0.78
		Wign01	**0.57**	**11.60**	−5.08	0.65
		Texture dependent	0.55	13.72	21.86	1.07
Wang	Jackson	Choudhury	0.53	11.94	−21.60	0.46
		Wign07	0.56	11.90	−1.96	0.73
		Wign01	0.56	11.67	−8.78	0.61
		Texture dependent	0.56	13.32	13.84	**0.96**
	Kirdyashev	Choudhury	0.55	11.81	−20.92	0.46
		Wign07	0.55	12.23	3.33	0.77
		Wign01	0.56	11.74	−4.46	0.62
		Texture dependent	0.48	14.63	24.74	1.05
	Wigneron	Choudhury	0.55	11.84	−19.86	0.47
		Wign07	0.56	12.03	**2.95**	0.80
		Wign01	**0.57**	**11.63**	−4.16	0.66
		Texture dependent	0.55	13.90	23.70	1.09

Table 4
Statistics of the global scale comparison between ECMWF CMEM simulations and SMOS observations of L-band brightness temperature at Y polarisation for a 40° incidence angle for 2010–2011 for 36 CMEM configurations if Set 1 experiments (see Table 1 nd 2). For each dielectric model best statistics are highlighted in bold. SDV is the normalised standard deviation (ratio between the simulated and observed TB standard deviations).

Dielectric Model	Vegetation Opacity Model	Soil Roughness Model	R	uRMSE (K)	Bias (K)	SDV
Dobson	Jackson	Choudhury	0.51	11.46	−12.11	0.48
		Wign07	0.52	11.66	−0.59	0.69
		Wign01	**0.53**	11.47	−3.57	0.62
		Texture dependent	0.51	13.07	11.16	0.94
	Kirdyashev	Choudhury	0.52	**11.38**	−12.12	0.49
		Wign07	0.50	11.91	2.62	0.73
		Wign01	0.52	11.54	−0.93	0.64
		Texture dependent	0.45	14.01	18.57	**1.02**
	Wigneron	Choudhury	0.52	11.41	−11.01	0.49
		Wign07	0.51	11.79	2.37	0.75
		Wign01	0.52	11.49	**−0.51**	0.66
		Texture dependent	0.49	13.57	17.81	1.06
Mironov	Jackson	Choudhury	0.52	11.42	−12.92	0.48
		Wign07	0.52	11.60	−2.69	0.69
		Wign01	**0.53**	11.39	−5.55	0.62
		Texture dependent	0.52	13.02	7.24	**0.94**
	Kirdyashev	Choudhury	**0.53**	**11.34**	−13.10	0.50
		Wign07	0.51	11.93	**0.04**	0.75
		Wign01	0.52	11.52	−3.32	0.66
		Texture dependent	0.46	14.16	13.78	**1.06**
	Wigneron	Choudhury	0.52	11.37	−11.93	0.49
		Wign07	0.52	11.75	−0.00	0.75
		Wign01	**0.53**	11.43	−2.75	0.67
		Texture dependent	0.50	13.60	13.35	1.07
Wang	Jackson	Choudhury	0.52	11.42	−12.71	0.48
		Wign07	0.52	11.71	−2.10	0.71
		Wign01	**0.53**	11.44	−5.06	0.63
		Texture dependent	0.51	13.23	8.21	0.97
	Kirdyashev	Choudhury	**0.53**	**11.34**	−12.91	0.50
		Wign07	0.51	12.05	0.61	0.77
		Wign01	0.52	11.56	−2.85	0.67
		Texture dependent	0.46	14.38	14.72	**1.09**
	Wigneron	Choudhury	0.52	11.37	−11.73	0.50
		Wign07	0.51	11.88	**0.60**	0.78
		Wign01	**0.53**	11.49	−2.25	0.69
		Texture dependent	0.49	13.87	14.34	1.11

system. A key assumption for data assimilation is that model and observations are unbiased, with random zero-mean errors (Yilmaz and Crow, 2013; Dee, 2005). However, in reality, systematic differences exist between modelled and observed radiances. They are caused by a number of reasons such as problems with the data, representativeness issues, forward model approximations, simplified representation of the processes. So, it is of crucial importance to correct for the systematic differences between the model and the observations prior to data assimilation. De Lannoy et al. (2013) and De Lannoy and Reichle (2015) calibrated their forward model parameters by minimising the bias in the mean and variance between multi-year simulated and observed SMOS TBs across incidence angles and polarisations. This calibration approach correct for the long term biases, but seasonal and shorter term Tb biases at individual incidence angles and polarisations still need to be corrected within the data assimilation system, as discussed in De Lannoy and Reichle (2015, 2016).

Cumulative Distribution Function matching (CDF-matching) methods allow to match the statistical moments of the observational data to the model ones, typically mean, variance, skewness and kurtosis (Reichle and Koster, 2004; Drusch et al., 2005). Scipal et al. (2008) proposed a simplified CDF-matching that relies on a linear approach to correct for the first two moments of the CDF (mean and variance). The simplified CDF-matching has been largely used by the land surface community showing that it efficiently removes the differences between model and observations for the first two moments of the CDF (Albergel et al., 2019; Barbu et al., 2014; Scipal et al., 2008). As pointed out by Barbu et al. (2014); Draper et al. (2012) there are also systematic differences between the seasonal cycles of models and observations. Not accounting for these seasonal scale systematic discrepancies would affect the matching at both short and seasonal time scales.

In this paper we use a grid-point based rescaling similar to the

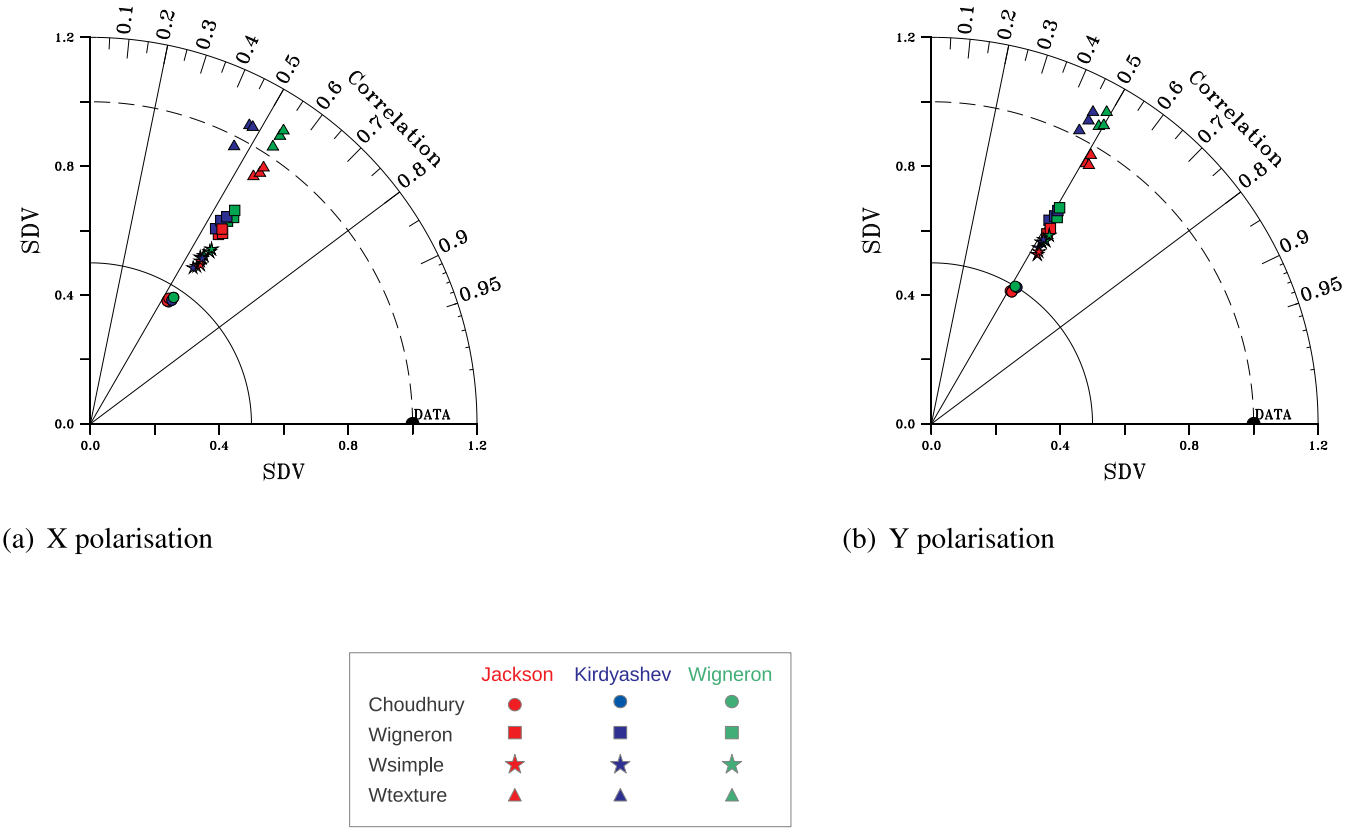

Fig. 3. Comparison between ECMWF simulated and SMOS measured TBs at L-band (1.4 GHz) at X (left) and Y (right) polarisations, for 2010–2011 for 36 CMEM configurations of Set 1 experiments (see Tables 1 and 2). Symbols colour and shapes represent different vegetation opacity and roughness models, respectively; and for each three identical symbols are used for the different dielectric models. (For interpretation of the references to colour in this figure legend, the reader is referred to the Web version of this article.)

simplified CDF-matching approach described by (Scipal et al., 2008). However we apply it at the monthly scale to remove the seasonally varying systematic biases between SMOS and ECMWF brightness temperatures, and we use a different set of rescaling coefficients at each incidence angle and polarisation. We use the 4-year (2010–2013) monthly climatology of observations and forward simulations, at 40 km resolution of experiments of Set 2 (Table 2). Using a 3-month moving window, we compute, for each calendar month from January to December, the mean 2010–2013 statistical moments (mean and variance) of the observed (T_{Bsmos}) and simulated (T_{Becm}) TBs. So, the approach accounts for the seasonal cycle but not for the inter-annual variability. The moments are computed separately at each grid point, at each polarisation, and for each incidence angle of 30°, 40° and 50° and for each month. At each grid point location and for each polarisation, incidence angle and multiyear 3-month window, a minimum of 50 model and observation values remaining after quality control (sections 2.1 and 2.4) is required to compute the moments. The statistical moments are then used to compute a set of monthly maps of rescaling parameters (A,B) for each X and Y polarisations, and for each 30°, 40° and 50° incidence angles. They are used to transform the observed SMOS observations for assimilation purposes as:

$$T^{\star}_{Bsmos} = A + B \cdot T_{Bsmos} \tag{8}$$

with

$$A = \langle T_{Becm} \rangle - \langle T_{Bsmos} \rangle \cdot \frac{StDev(T_{Becm})}{StDev(T_{Bsmos})} \tag{9}$$

$$B = \frac{StDev(T_{Becm})}{StDev(T_{Bsmos})} \tag{10}$$

The first parameter, A, is considered as a bias correction parameter and the second parameter, B, as a rescaling slope parameter. The obtained matching parameters and results of the seasonal bias correction approach are presented in section 3.2.

3. Results

3.1. CMEM global intercomparison

Global maps of 2010–2011 mean TBs at X and Y polarisations are given in Fig. 1, (a) as observed from SMOS and (b) simulated from one of the experiments of Set 1 (see Tables 1 and 2): the one using Wang for the dielectric model, the Wigneron et al. (2001) soil roughness model and the Wigneron vegetation model and using input data as described in Section 2.3. Fig. 1(c) shows the mean first guess departure (observation minus model) TB at each polarisation. Fig. 2 presents, maps of root mean square error (RMSE), unbiased RMSE (uRMSE) and correlation for the same period and experiment. Mean values of SMOS TB at X polarisation typically range between 240 K and 280 K in most areas (Fig. 1(a)), with colder mean TBs at high latitude. As expected, measured SMOS TBs are larger at Y than at X polarisation, in particular over warm desert areas with up to 300 K mean values for 2010–2011. Fig. 1(b,c) shows that forward simulations using this configuration of CMEM tend to overestimate TB values at both X and Y polarisations by up to 20 K, specially in dry areas, but also in North America and India, and to underestimate them over tropical forest areas and at high latitudes.

The top panel of Fig. 2 indicates relatively large RMSE values often between 16 K and 30 K at X and Y polarisations matching relatively well areas with large bias shown in Fig. 1(c). Maps of uRMSE, Fig. 2(b),

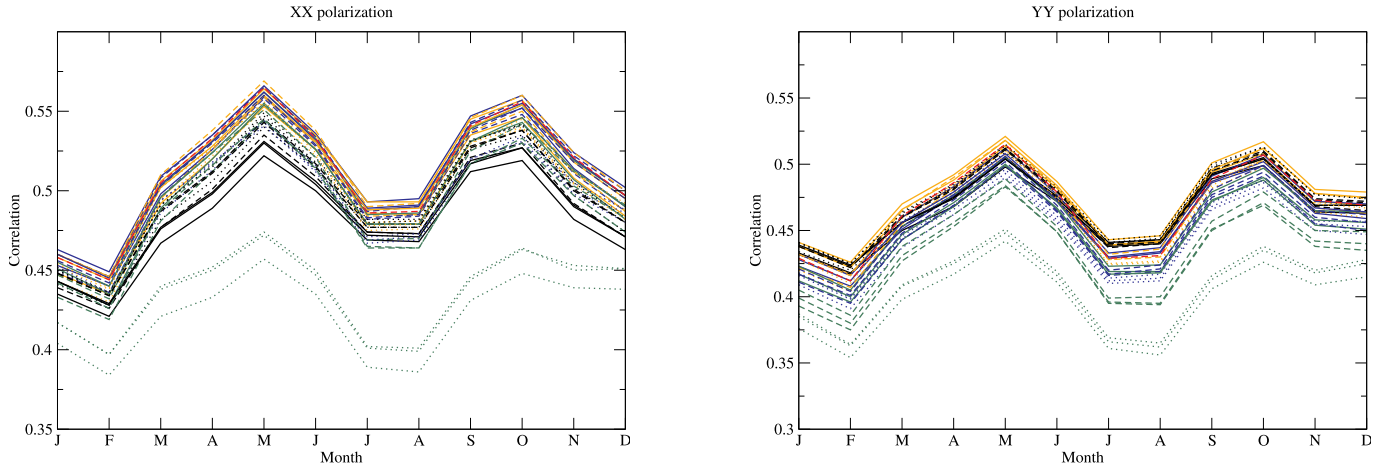

(a) Correlation

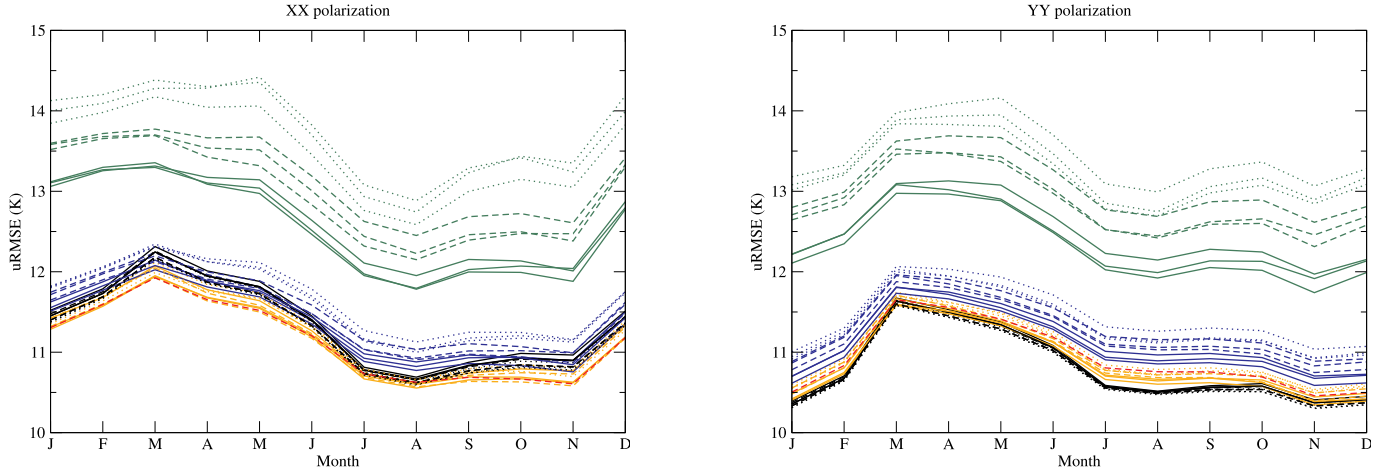

(b) Unbiased RMSE

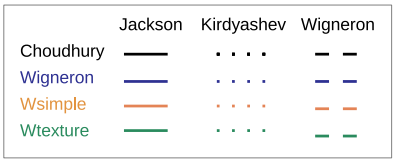

Fig. 4. Annual cycle of the global mean correlation (top) and URMSE (bottom) between L-band TBs observations from SMOS and ECMWF forward simulations for the 36 CMEM configurations of Set 1 experiments (see Tables 1 and 2), at X (left) and Y (right) polarisations, for a 40° incidence angle. Statistics are computed on the period 2010–2011.

show much lower values than for RMSE, indicating the large contribution of the bias to the RMSE for this configuration of CMEM. Areas with uRMSE larger than 16 K remain in Asia and Eastern Europe. These areas are known to be affected by RFI sources leading to unreliable SMOS measurements. Pixels contaminated by RFI are not systematically accurately flagged out in the SMOS product. Residual SMOS measurements affected by RFI are in strong disagreement with the simulated values, explaining large uRMSE in these regions. The bottom panel of Fig. 2 shows that SMOS measurements and CMEM forward simulations are well correlated for 2010–2011, with values larger than 0.4 in most areas. This shows good agreement between simulated and observed TBs seasonal and sub-seasonal cycles, which is remarkable as they result from combined temperature, soil moisture and vegetation water content evolution. Lowest correlation values are shown in grey in tropical forests areas. They are due to the relative stable TBs in these areas, with low temporal dynamics in both the model and the observations, leading to low correlation. Low correlation values are also shown in RFI affected areas of Asia. Global mean statistics for this configuration of CMEM indicate correlation values of 0.57 and 0.53 at X and Y polarisation, respectively. Values of uRMSE are 11.63 K and 11.49 K.

Global mean 2010–2011 statistics are provided in Tables 3 and 4 for each of the 36 experiments of Set 1 corresponding to different configurations of CMEM. They include correlation, uRMSE, bias and SDV, which is the normalised standard deviation, i.e the ratio between the

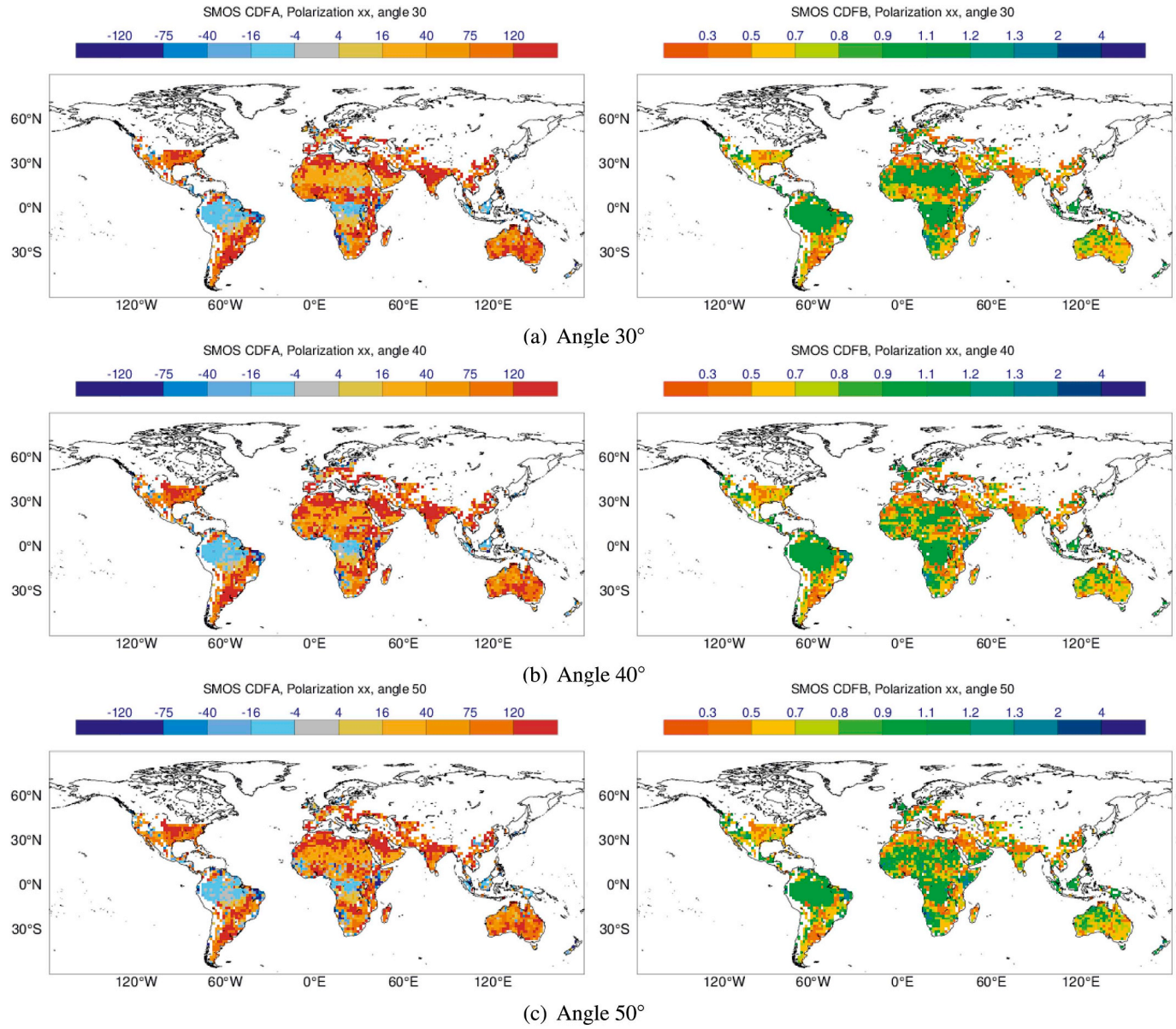

Fig. 5. ECMWF monthly rescaling parameters A in K (left) and B (right), for January, at X polarisation, computed at 40 km resolution, at 30° (top panel), 40° (middle panel) and 50° (bottom panel), for the default CMEM configuration using the dielectric model of Wang and Schmugge, the simple soil roughness Model of Wigneron et al. (2001) and the Wigneron et al. (2007) vegetation opacity model.

simulated and observed TB standard deviations. The results of these two Tables are also summarised in Taylor diagrams (Taylor and Clark, 2001) given in Fig. 3, whereas the annual cycles of uRMSE and correlation statistics are shown in Fig. 4. The Taylor diagrams show averaged statistics, so the classic relationship between E, R and SVD found in Taylor diagrams is not strictly valid, however they clearly illustrate model performances shown in the Tables.

In this paper, the primary criteria of evaluation to select best CMEM parameterizations are correlation and uRMSE metrics, whereas bias and SDV results are secondary criteria. This is because NWP applications, including monitoring and assimilation, apply an a priori a bias correction to match the mean and the variance of model and observed TBs (Section 2.5).

Results of Tables 3 and 4 and Fig. 3 all clearly show that the choice of the roughness parameterisation has the largest impact on correlation, uRMSE, bias and SDV statistics. The texture dependent soil roughness model, when it is used in combination with the Kirdyashev vegetation model, tend to show poorer correlation and poorer uRMSE performances than the other parameterisations. This result is persistent across the annual cycle as shown by Fig. 4. Results from the two tables and the Taylor diagrams show however that experiments using the texture dependent roughness model best capture the SMOS TB standard deviation, with SDV values close to 1. The other roughness parameterisations lead to SDV values lower than 1, indicating that they underestimate the variance compared to the SMOS data. As described in Sections 2.2 and 2.3, the forward model uses H-TESSEL input, with a 7 cm top soil layer, which is in most situations larger than the SMOS sensing depth. In turn, the SMOS data with a shallower sensing depth is expected to capture larger standard deviation, related to highly variable surface soil moisture, than the model, which explains that most roughness models underestimate SDV. The Wigneron 2007 and Wigneron (2001) roughness parameterisations better match the SMOS data than the soil texture dependent roughness (Kerr et al., 2010a) or Choudhury (Choudhury et al., 1979) models in terms of correlation, uRMSE and bias. And looking into more details at the Wigneron (2001) and Wigneron (2007) statistics, results show that Wigneron (2001)

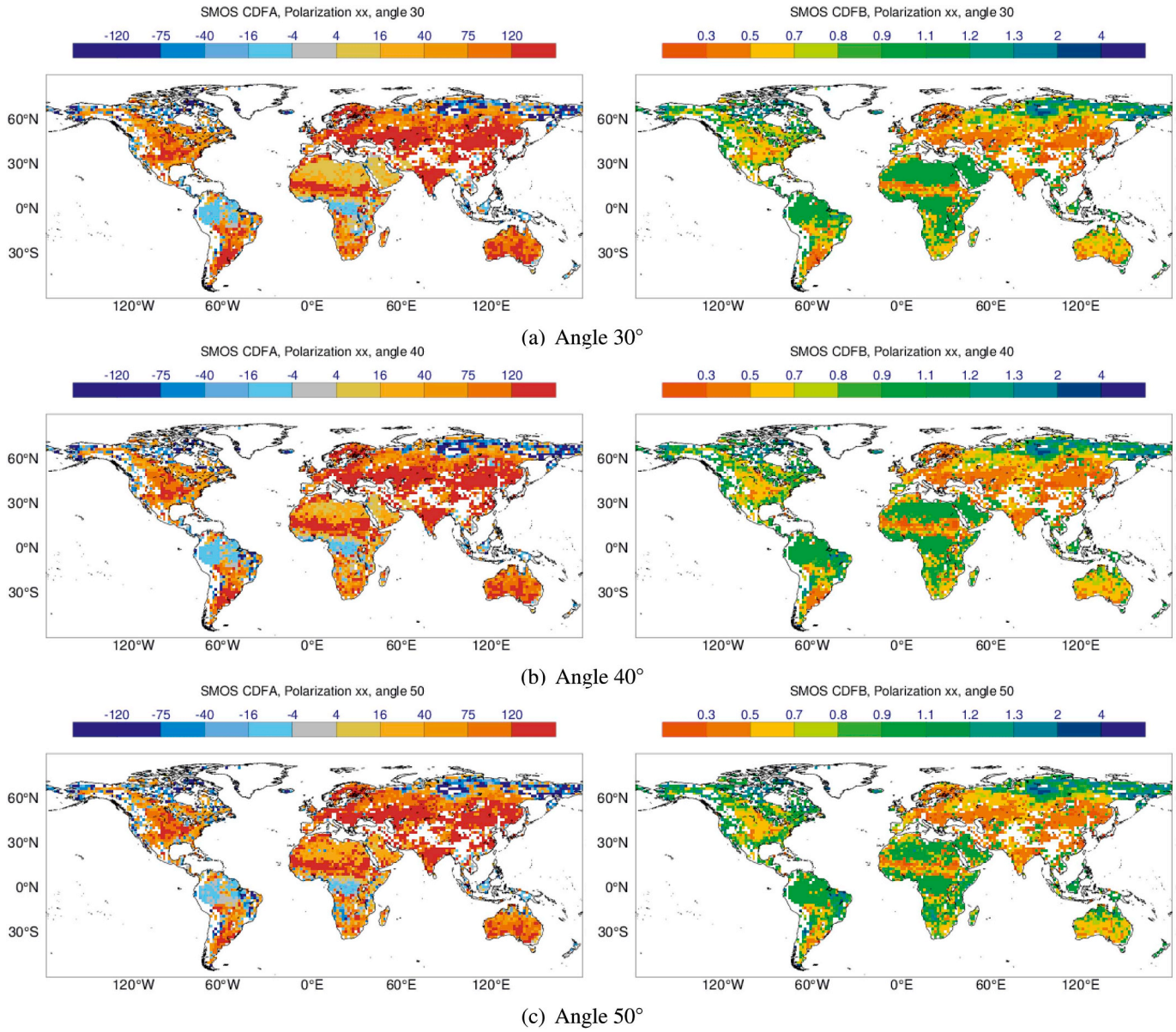

Figure 6. ECMWF monthly rescaling parameters A in K (left) and B (right), for July in X polarisation, computed at 40 km resolution, at 30° (top panel), 40° (middle panel) and 50° (bottom panel), for the default CMEM configuration using the dielectric model of Wang and Schmugge, the simple soil roughness Model of Wigneron et al. (2001) and the Wigneron et al. (2007) vegetation opacity model.

leads to lower uRMSE and larger correlation than the Wigneron (2007) roughness model.

For the vegetation optical depth, statistics given in Tables 3 and 4 show that Jackson and Wigneron perform better than Kirdyashev in terms of correlation and uRMSE. This result differs from the results obtained at C-band by de Rosnay et al. (2009a) who showed that Kirdyashev was performing better than Jackson or Wigneron over West Africa. Result obtained here at L-band are not surprising as Jackson and Wigneron parameterisations were developed for L-band, so they are best suited for SMOS applications, whereas Kirdyashev is a multi-frequency model. The Wigneron vegetation opacity parameterisation tend to show slightly better statistics than Jackson in terms of uRMSE.

Simulated TBs are less sensitive to the dielectric model than to the vegetation opacity and soil roughness models. Evaluated against SMOS observations, performances of the Wang and Schmugge and the Mironov soil dielectric models are similar and better than with the Dobson model. The Wang and Schmugge model is used in the following sections of the paper, along with the Wigneron simple roughness and vegetation models. This combination of CMEM options also defines the CMEM v5.1 default configuration which was released by ECMWF based on these results.

3.2. Bias correction results

Figs. 5 and 6 show the maps of rescaling parameters (Section 2.5) at X polarisation, for 30°, 40° and 50° incidence angles, for January and July, respectively, using the 2010–2013 data sets (see Table 2). Both the bias correction term *A* and the rescaling term *B* show a relatively good consistency across the different incidence angles. The bias correction parameter *A* has generally positive values in desert areas, in particular in Sahara and Australia, which are consistent with the departure results presented at 40° in Fig. 1 for 2010–2011 at coarser resolution. In January, Fig. 5 shows that large areas in the northern hemisphere do not have any rescaling parameters due to quality control rejecting frozen and snow covered areas in the winter hemisphere. In both January and July, areas with complex topography (e.g. in the US Rocky mountains,

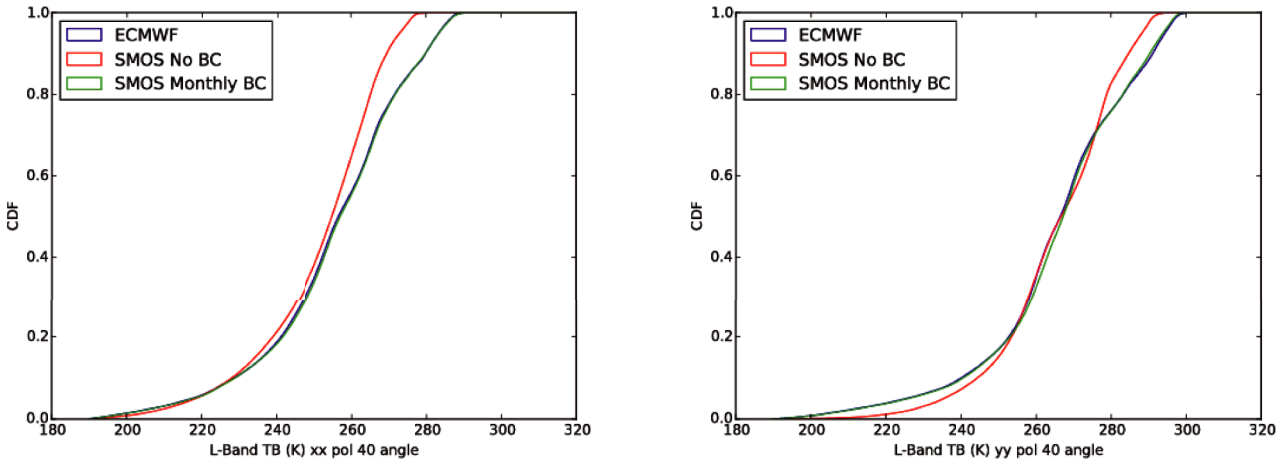

(a) X pol (b) Y pol

Fig. 7. Global and temporal Cumulative Distribution Function of SMOS observed (red), ECMWF reanalysed (blue) and SMOS monthly rescaled SMOS (green) TBs (K) for 2013 at X pol (left) and Y pol (right) at 40° incidence angle. (For interpretation of the references to colour in this figure legend, the reader is referred to the Web version of this article.)

The Andes, the Alpes and parts of the Himalayan mountains) are masked out. The figures also show that regions in China are masked out, which is due to RFI filtering.

These rescaling parameters are applied to the ERA-Interim based CMEM forward simulations conducted for 2010–2013, for experiments of Set 2 as detailed in Section 2.

Global CDFs of TBs for the year 2013 are presented in Fig. 7, at X polarisation (left) and Y polarisation (right), at 40° incidence angle for ECMWF CMEM forward simulations (blue), SMOS observations before bias correction (red) and SMOS observations after bias correction (green). The figure shows that the multi-angular polarised monthly bias correction approach allows to effectively match the cumulative distributions of the observed and simulated TBs.

Fig. 8 provides detailed examples of time series and CDF of ECMWF CMEM simulations and SMOS observations before and after bias correction in two areas of Australia (25S–35S; 140E-150E), and South America (15S–20S; 50W–45W) for 2013. As shown in the time series presented in the top panel of Fig. 8, in Australia, the SMOS observations before bias correction (red) are colder that the ECMWF CMEM forward simulations, as already pointed out with the global maps shown in Fig. 9. The figure also points out that the annual cycle and the shorter time scale variability are captured by the observations and the model (which is consistent with Fig. 10 for this area). There are several occurrences of strong decrease in TB, typically corresponding to precipitation events and increased soil moisture, observed and simulated around day 25 and 60 and 145. It is clear from this figure that the SMOS observations have a larger variability than the model forward simulations as expected and as discussed in the previous subsection, partly due to the model parameter settings as well as a shallower SMOS sampling depth than the ECMWF model top layer thickness. For example on days 90 and 145, the amplitude of the SMOS signal is larger than that of ECMWF. On a single event, it could be attributed to a number of reasons, such as for example a lack of precipitation in the ECMWF system leading to an underestimation of soil moisture increase. However, the fact that the SMOS variability is systematically larger than the ECMWF forward simulations is consistent with model top layer and SMOS sampling depth mismatch and the fact that the model uses uniform vertical soil moisture profile in the top layer (Wilker et al., 2006). One of the purposes of bias correction is specifically to correct for model approximations that lead to systematic differences (Dee, 2005). After bias correction, the SMOS data is in general better agreement with the model at the seasonal scale with remaining differences at the daily scale and precipitation event scale which are of potential relevance for data assimilation purpose (green curve of the top panel of Fig. 8). In South America (bottom panel of Fig. 8) the observed and simulated TB are already in relatively good agreement before bias correction, both in terms of mean value and variability. For both regions of Fig. 8, the right panels show that the CDF are efficiently matched at the regional scale.

Tables 5 and 6 give an overview of the yearly statistics of the ECMWF CMEM forward simulations and the SMOS TBs observations for each incidence angle, each polarisation for all years between 2010 and 2013. They indicate the 95% Confidence Interval (CI) computed for each correlation using a Fisher Z transform. Before bias correction (Table 5), depending on the incidence angle and the year, RMSE values range between 16.96 K and 20.64 K at X polarisation and between 12.77 K and 17.30 K at Y polarisation, with mean value for all polarisations and incidence angles of 16.67 K. These mean statistics hide large spatial scale differences as shown in Figs. 9 and 10. Correlation values are on average 0.56, varying between 0.51 and 0.60 at X polarisation, and between 0.49 and 0.64 at Y polarisation, with large confidence interval for each angle, polarisation and year. Anomaly correlations are computed based on time series obtained by removing the seasonal cycle based on a 4-month moving window with an averaged value of 0.31. The Mean Absolute Bias (MAB) has an average value of 11.04 K. After bias correction, the mean correlation, RMSE and MAB are improved to 0.62, 7.91 K and 1.39 K, respectively. The anomaly correlation remain very close to its value before bias correction, 0.31, which is as expected since the seasonal bias correction approach preserves the SMOS signal short term variability.

The impacts of using the 2010–2013 rescaling coefficients on the SMOS-CMEM differences for the 2014–2016 period is shown in Table 7 at 40° incidence angle. Results show that correlation and anomaly correlation values are very close before and after bias correction. However mean absolute bias and RMSE are drastically reduced after bias correction compared to before bias correction. Although the residual mean absolute bias is slightly larger than for the 2010–2013 period, it is lower than 3 K instead of more than 11 K and 8 K before bias correction at X and Y polarisations, respectively. RMSE is reduced from values above 17 K and 13 K at X and Y polarisations before bias correction, to less than 9 K at both polarisations after bias correction. On average, the 2014–2016 global RMSE is reduced from 15.56 K before bias correction, to 8.19 K after bias correction, and the mean

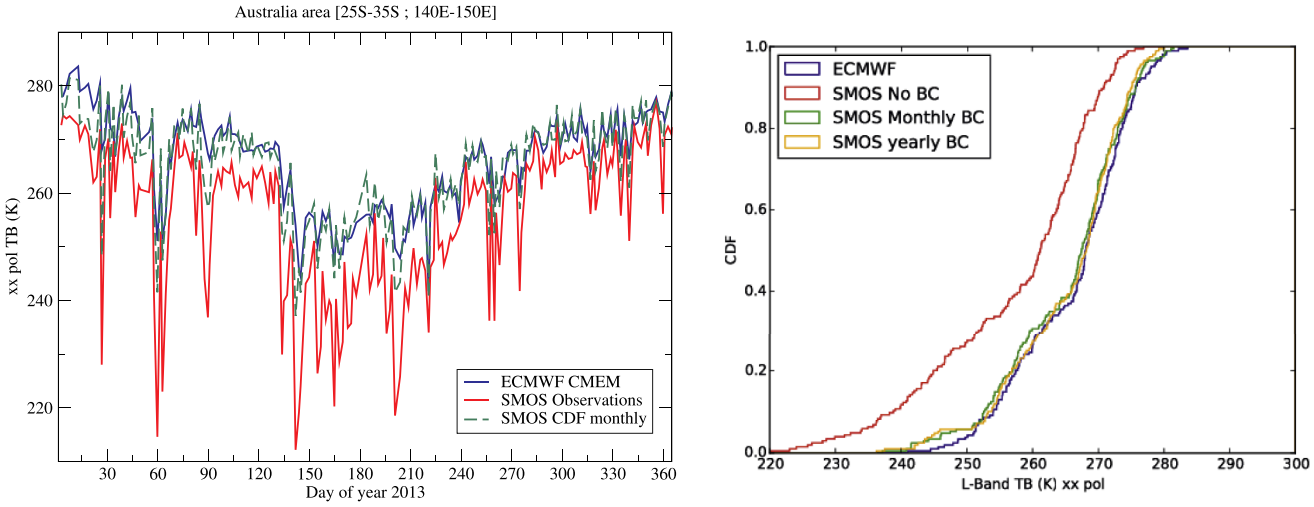

(a) Australia

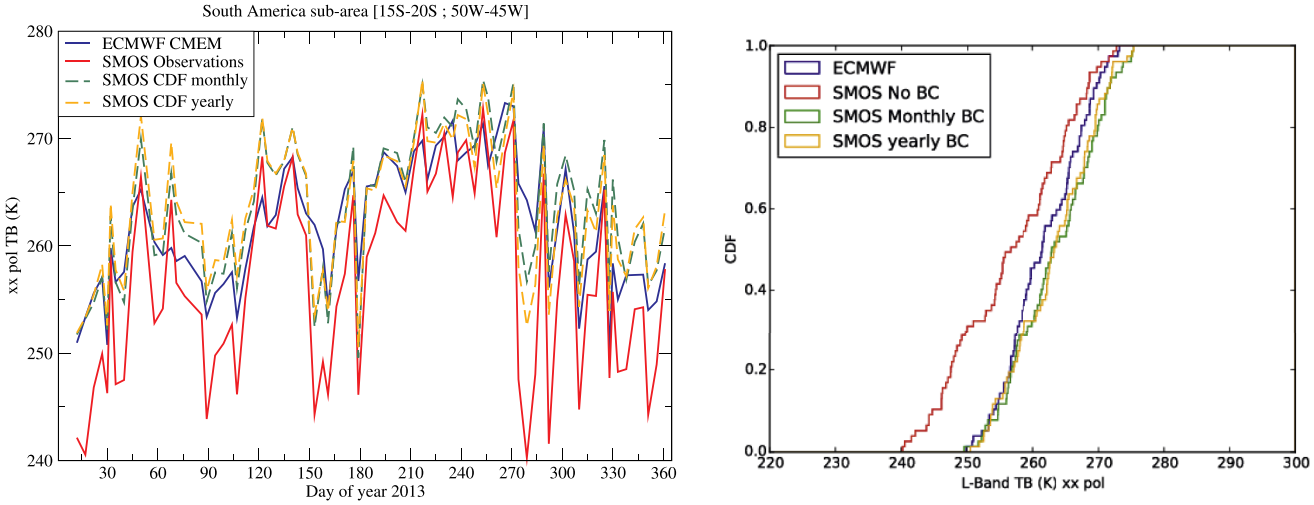

(b) South America

Fig. 8. Annual cycle (left) and CDF (right) for 2013 of X pol TB (in K), at 40° incidence angle, simulated by ECMWF CMEM (blue), observed by SMOS (red) and matched using monthly rescaling (green), and annual rescaling (yellow) for two areas located in Australia (a) and South America (b). (For interpretation of the references to colour in this figure legend, the reader is referred to the Web version of this article.)

absolute bias from 10.16 K to 2.51 K, with no impact on the correlation values that remain at 0.61 in both cases.

Maps of RMSE and mean difference between SMOS observations and ECMWF CMEM forward simulations at 40° incidence angle, for 2015 computed before (left) and after (right) bias correction are given in Fig. 9. Before bias correction, RMSE values typically range between 16 K and 20 K (red colours). After bias correction RMSE values are in the range of 4 K to 8 K in most areas. The annual mean bias is also reduced to a residual value lower than 3 K in most areas. Fig. 10 presents maps of correlation and standard deviation before and after bias correction for 2015. The top-left panel of Fig. 10 indicates very good correlation values between SMOS observations and CMEM even before bias correction. In North America and in parts of Australia, correlation values larger than 0.8 dominate. The bias correction, because it relies on a monthly approach, further improves the agreement between the SMOS observations and CMEM at the seasonal scale, leading to increased correlation values after bias correction, with extended areas with correlation values larger than 0.8 in North America, in Sahel, in Siberia and parts of Europe (top right of Fig. 10).

Histograms of global scale SMOS first guess departure (observations minus model) are presented in Fig. 11 before and after bias correction, at 40° incidence angle at X polarisation and Y polarisation, for 2015. Before bias correction (in red) the distributions are uncentered, with a relatively large spread, which illustrate systematic differences between the observations and the model at all incidence angles and polarisations. The monthly bias correction (in green) leads to narrow and centred first guess departure distributions, validating the bias correction approach using independent observations.

3.3. Long term SMOS monitoring

Long term global scale spatial averaged monitoring statistics are presented in Fig. 12. They are obtained at a 40° incidence angle, from 2010 to 2016 using the ERA-Interim-based CMEM forward simulations of Set 3 described in Table 2 and the SMOS TB measurements for the entire period as described in Section 2.1. The left panel shows that at

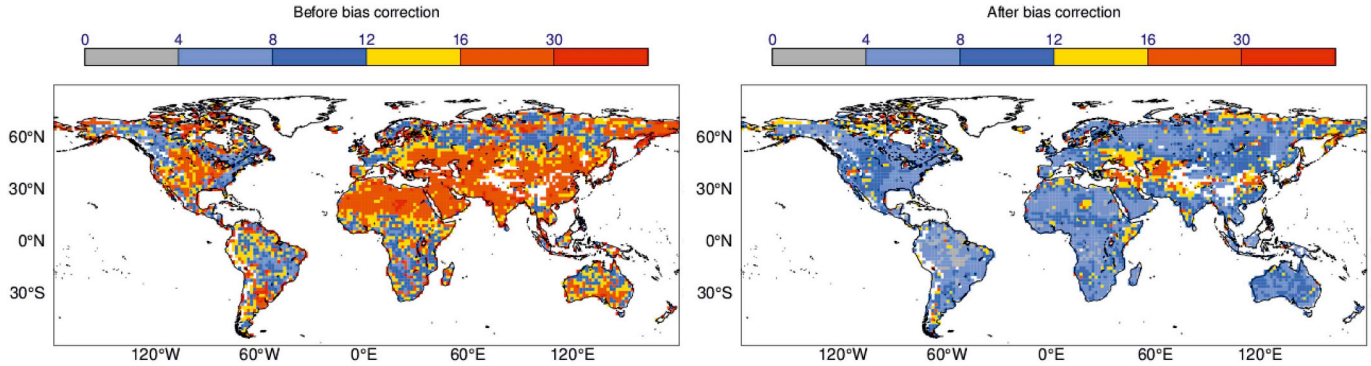

(a) RMSE (K)

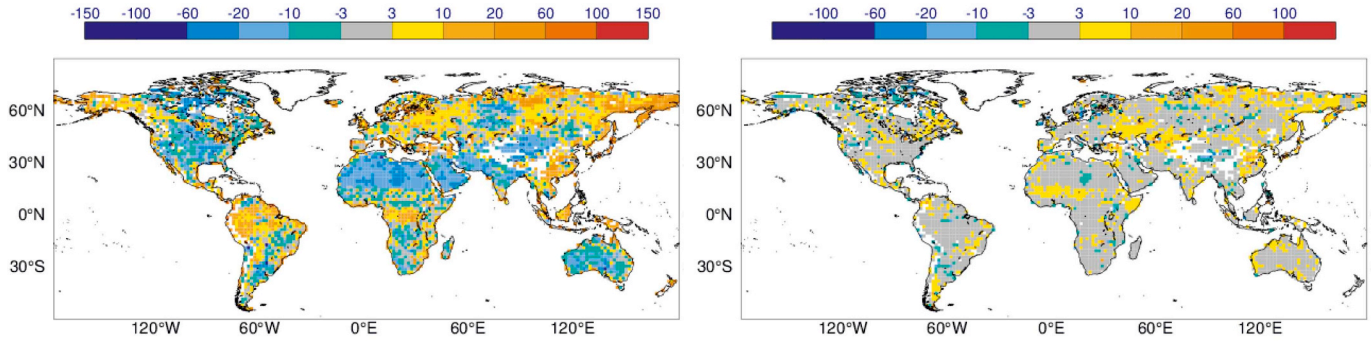

(b) Bias (Observation - Model) (K)

Fig. 9. Comparison between ECMWF CMEM and SMOS TBs before (left) and after (right) bias correction, for 2015, at X pol and 40° incidence angle. Panels a and b show RMSE (K) and bias (K), respectively.

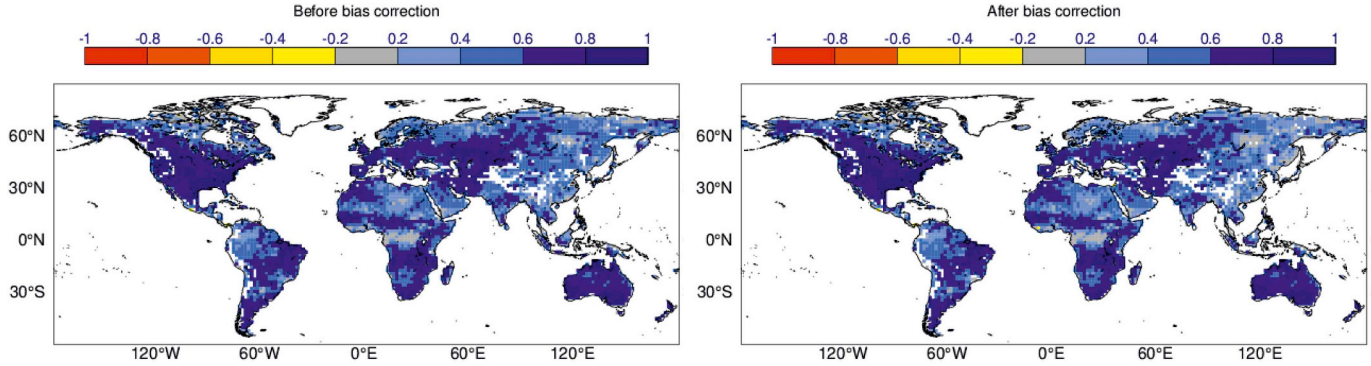

(a) Correlation

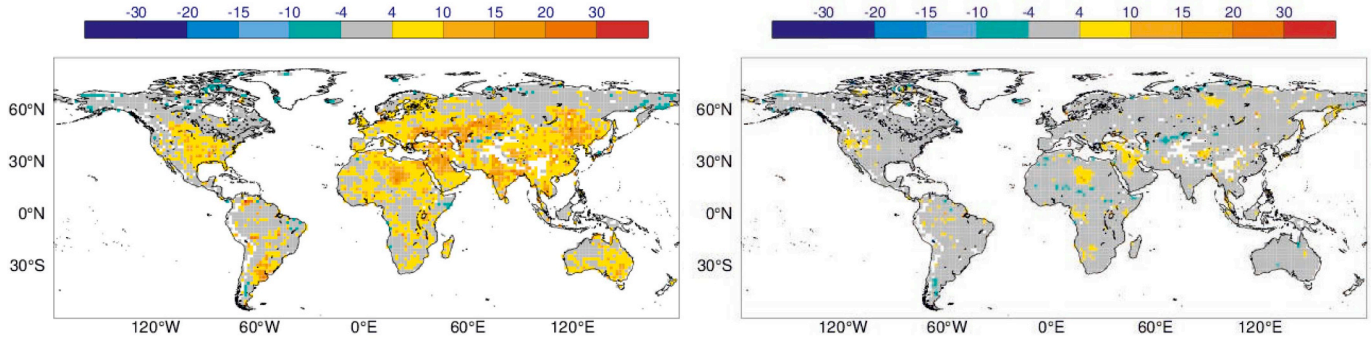

(b) STD difference (Observation - Model) (K)

Fig. 10. Comparison between ECMWF CMEM and SMOS TBs before (left) and after (right) bias correction for 2015, at X pol and 40° incidence angle. Panel a shows correlation and panel b shows differences in STD (K).

Table 5
Statistics of the global scale comparison, before bias correction, between the ECMWF CMEM Set 2 experiment, using the Wang and Schmugge dielectric model, the Wigneron (2001) roughness model and the Wigneron (2007) vegetation model (see Tables 1 and 2), and SMOS observations of L-band TB at X and Y polarisations for 30°, 40°, 50° incidence angles, for 2010–2013.

Angle	Year	pol	N	R	Confidence		Anomaly R	RMSE (K)	MAB (K)
30	2010	X	101.63	0.57	0.43	0.69	0.32	18.06	12.23
30	2011	X	106.86	0.59	0.45	0.70	0.32	17.53	12.11
30	2012	X	94.66	0.59	0.44	0.71	0.33	17.11	11.74
30	2013	X	101.44	0.60	0.46	0.72	0.34	16.96	11.87
40	2010	X	150.17	0.57	0.45	0.67	0.34	18.62	12.71
40	2011	X	157.68	0.58	0.46	0.68	0.35	18.04	12.56
40	2012	X	139.84	0.58	0.46	0.68	0.36	17.61	12.21
40	2013	X	149.58	0.60	0.48	0.69	0.37	17.38	12.29
50	2010	X	148.28	0.51	0.37	0.62	0.27	20.64	14.68
50	2011	X	155.76	0.51	0.38	0.62	0.27	20.02	14.67
50	2012	X	138.50	0.52	0.38	0.63	0.27	19.57	14.11
50	2013	X	147.69	0.53	0.41	0.64	0.28	19.33	14.27
30	2010	Y	101.00	0.58	0.43	0.69	0.33	17.30	11.23
30	2011	Y	106.34	0.60	0.46	0.71	0.36	16.30	10.78
30	2012	Y	94.44	0.62	0.47	0.73	0.39	15.34	10.16
30	2013	Y	101.11	0.64	0.50	0.74	0.40	14.81	10.00
40	2010	Y	146.74	0.53	0.40	0.64	0.27	16.27	9.72
40	2011	Y	154.41	0.54	0.42	0.65	0.28	15.46	9.34
40	2012	Y	136.88	0.56	0.43	0.66	0.30	14.49	8.72
40	2013	Y	146.83	0.58	0.46	0.68	0.31	13.97	8.54
50	2010	Y	140.68	0.49	0.35	0.61	0.24	15.14	8.49
50	2011	Y	147.65	0.50	0.37	0.61	0.24	14.26	8.01
50	2012	Y	130.59	0.53	0.39	0.64	0.27	13.29	7.43
50	2013	Y	140.27	0.54	0.41	0.65	0.28	12.77	7.18

Table 6
Statistics of the global scale comparison, after bias correction, between the ECMWF CMEM Set 2 experiment, using the Wang and Schmugge dielectric model, the Wigneron (2001) roughness model and the Wigneron (2007) vegetation model (see Tables 1 and 2), and SMOS observations of L-band TB at X and Y polarisations for 30°, 40°, 50° incidence angles, for 2010–2013.

Angle	Year	pol	N	R	Confidence		Anomaly R	RMSE (K)	MAB (K)
30	2010	X	102.08	0.64	0.50	0.74	0.31	7.95	−0.36
30	2011	X	107.54	0.65	0.52	0.75	0.32	7.46	0.20
30	2012	X	95.69	0.65	0.51	0.75	0.32	7.42	0.50
30	2013	X	101.74	0.67	0.54	0.76	0.34	7.09	0.24
40	2010	X	151.29	0.63	0.52	0.72	0.34	8.04	−0.42
40	2011	X	159.04	0.64	0.54	0.73	0.35	7.53	0.18
40	2012	X	141.95	0.65	0.54	0.73	0.35	7.48	0.55
40	2013	X	150.50	0.67	0.56	0.75	0.37	7.13	0.35
50	2010	X	148.95	0.57	0.44	0.67	0.26	8.96	−0.33
50	2011	X	156.65	0.58	0.46	0.67	0.26	8.50	0.12
50	2012	X	139.98	0.58	0.46	0.68	0.27	8.41	0.50
50	2013	X	148.16	0.60	0.48	0.70	0.28	8.05	0.33
30	2010	Y	100.90	0.63	0.50	0.74	0.33	8.53	−0.76
30	2011	Y	106.17	0.66	0.53	0.76	0.35	7.64	−0.13
30	2012	Y	94.79	0.68	0.55	0.77	0.39	7.14	0.37
30	2013	Y	100.76	0.70	0.58	0.79	0.40	6.76	0.32
40	2010	Y	147.16	0.58	0.46	0.68	0.27	8.90	−0.84
40	2011	Y	154.34	0.60	0.49	0.69	0.28	8.16	−0.15
40	2012	Y	137.43	0.62	0.50	0.71	0.30	7.68	0.28
40	2013	Y	146.12	0.64	0.53	0.73	0.31	7.26	0.32
50	2010	Y	139.51	0.54	0.41	0.65	0.25	9.43	−1.17
50	2011	Y	145.79	0.56	0.43	0.66	0.25	8.66	−0.36
50	2012	Y	129.31	0.58	0.45	0.69	0.28	8.07	0.14
50	2013	Y	137.93	0.60	0.47	0.70	0.29	7.75	0.16

both polarisations, correlations and anomaly correlation statistics steadily improve between 2010 and 2016. The correlation values increase from 0.57 to 0.63 at X polarisation and from 0.53 to 0.63 at Y polarisation. Although the improvement remains in the 95% confidence interval (see Tables 5–7) the improvement is consistent from 2010 to 2016. The anomaly correlation values also increase from 0.34 to 0.40 and from 0.27 to 0.37 at X and at Y polarisations, respectively. The right panel shows that the RMSE and uRMSE values decrease from 2010 to 2016 at both polarisations. The RMSE values range from 18.62 K in 2010 to 17.12 K in 2016 at X polarisation and from 16.27 K to 13.57 K at Y polarisation. For the uRMSE, the results show an improvement from 11.82 K to 10.46 K and from 11.75 K to 9.25 K at X and Y polarisations, respectively. These results are based on reanalysis based forward simulations, which are expected to be of nearly constant quality. Consistent SMOS TBs from the SMOS processor v5.05 are used until April 2015 and from the SMOS processor v6.20 after May 2015 (Section 2.1). So, the steady improvement shown from 2010 to 2014 is mostly due to SMOS observations improvement, possibly due to actions

Table 7
Statistics of the global scale comparison between ECMWF CMEM and SMOS observations at 40° incidence angle at X and Y polarisations before and after bias correction with the 2010–2013 bias correction coefficients applied to 2014–2016.

Angle	Year	pol	N	R	Confidence		Anomaly R	RMSE (K)	MAB (K)
Before BC	2014	X	161.57	0.61	0.50	0.70	0.37	17.23	11.93
	2015	X	157.69	0.61	0.50	0.70	0.38	17.51	11.97
	2016	X	142.04	0.63	0.52	0.72	0.40	17.12	11.92
	2014	Y	158.69	0.58	0.47	0.68	0.32	13.88	8.28
	2015	Y	154.41	0.60	0.49	0.70	0.34	14.03	8.50
	2016	Y	139.23	0.63	0.51	0.72	0.37	13.57	8.36
After BC	2014	X	162.85	0.60	0.49	0.69	0.37	8.20	2.11
	2015	X	159.28	0.60	0.49	0.70	0.38	8.75	2.94
	2016	X	142.85	0.63	0.52	0.72	0.40	8.43	2.93
	2014	Y	159.04	0.59	0.48	0.68	0.32	7.86	1.99
	2015	Y	155.10	0.60	0.49	0.70	0.34	8.05	2.51
	2016	Y	139.31	0.63	0.51	0.72	0.36	7.84	2.59

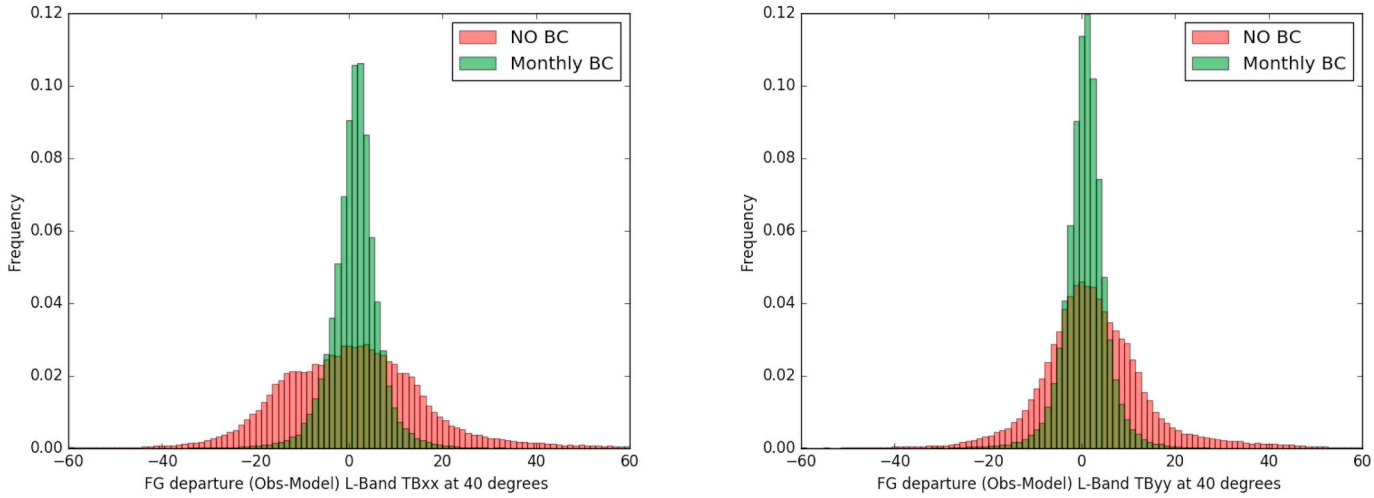

(a) First guess departure (Observation minus model) for July 2015

Fig. 11. Histograms of monthly mean first guess departures (Observation - Model in K) for July 2015 at 40° incidence angle, at X pol (left) and Y pol (right). Red and green colours show first guess departure distribution with no bias correction and with monthly bias correction, respectively. (For interpretation of the references to colour in this figure legend, the reader is referred to the Web version of this article.)

taken to manage RFI contamination (Mecklenburg et al., 2016; Kerr et al., 2016). Improvements for 2015–2016 result from combined SMOS processor improvements and possible RFI contamination decrease. Although the different contributions are difficult to disentangle these results clearly show an overall SMOS TB product quality substantial improvement at both polarisations between 2010 and 2016.

4. Summary and conclusion

This paper presented the SMOS forward modelling activities conducted at ECMWF to use the SMOS TB data. The first step was to develop and configure the observation operator CMEM. We evaluated different combinations of CMEM parameterisations against SMOS observations and to define CMEM's configuration for SMOS monitoring and data assimilation activities at ECMWF. To identify the best configuration of CMEM, 36 numerical experiments, using different combinations of three dielectric models, three vegetation opacity models and four roughness models, were conducted at 80 km resolution and at 40° incidence angle for 2010–2011. Experiments were conducted using ERA-Interim conditions as input of the land surface model H-TESSEL and the forward model CMEM. Results were evaluated against SMOS TB observations at both polarisations. They showed that simulated TBs are most sensitive to the soil roughness models, with less sensitivity to the dielectric model. Best CMEM results were obtained with the Wigneron model for the vegetation opacity and the simple Wigneron soil roughness model. For the soil dielectric model, performances of the Wang and Schmugge and the Mironov models were shown to be similar and better than with the Dobson model. The Wang and Schmugge model was used in the next steps of this paper, along with the Wigneron simple roughness and vegetation models. This combination of CMEM options defines the CMEM v5.1 default configuration which was released by ECMWF based on these results.

In a second step, we presented and evaluated the SMOS bias correction approach developed to use SMOS TB measurements for data assimilation purpose as investigated by Muñoz-Sabater et al. (2019). The paper described a multi-angular multi-polarised bias correction method based on a linear rescaling computed at the monthly scale using SMOS observations and ECMWF-CMEM re-analysed (ERA-Interim) TBs for a four year period (2010–2013). Experiments were conducted at 40 km resolution with and without bias correction and results were compared to the SMOS observations at global scale and at regional scale. Results showed that the seasonal multi-angular multi-polarisation bias correction approach reduces global RMSE to 7.91 K, compared to 16.7 K before bias correction, whereas the the mean absolute bias is reduced to 1.39 K (compared to 11.04 K before bias correction). The consistency between the simulated and the observed TBs seasonality is

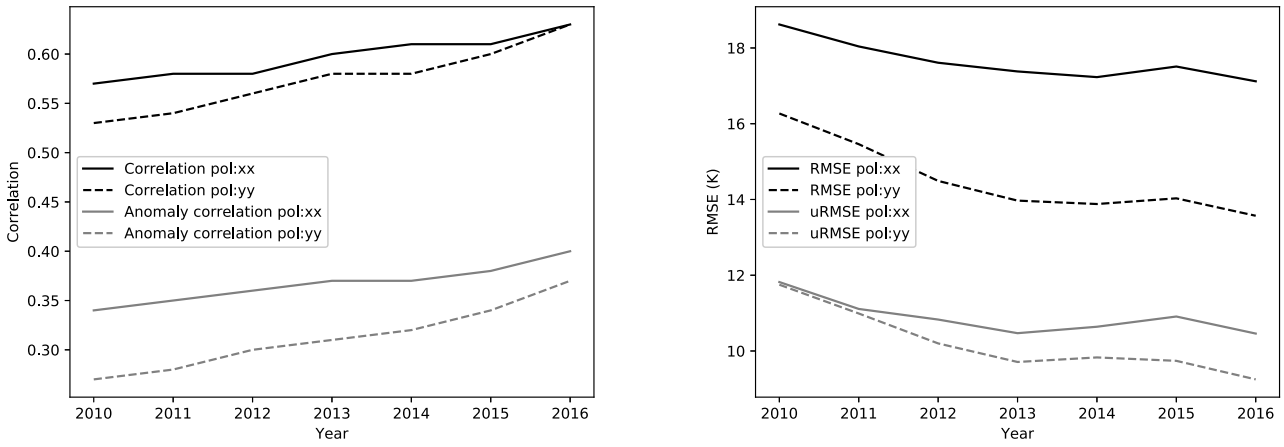

(a) Correlation (b) Root mean square error

Figure 12. Global mean statistics of SMOS TBs monitoring from 2010 to 2016, comparing SMOS observations to ECMWF CMEM reanalysis of L-Band TB, at 40° incidence angle, at X (solid line) and Y (dashed line) polarisations. Left panel depicts correlation (black) and anomaly correlation (grey). Right panel depicts RMSE (black) and uRMSE (grey).

also improved by using a monthly bias correction, leading to correlation values improvement to 0.62 after bias correction compared to 0.56 before. The 2010–2013 bias correction applied to the 2014–2016 period at 40° incidence reduces the global RMSE from 15.56 K before bias correction, to 8.19 K after bias correction, and the mean absolute bias from 10.16 K to 2.51 K, with no impact on the correlation values that remain at 0.61 in both cases. Some RFI can still be embedded in the product after filtering, however, remaining discrepancies between simulated and observed TBs are mostly random difference of relevance for future data assimilation studies.

Finally, long term monitoring statistics of SMOS observations were presented and analysed for an extended period covering 2010–2016, focusing on 40° incidence angle data. Results of the comparison with reanalysis-based forward simulations were presented. They showed that the consistency between SMOS and ECMWF reanalysis-based TBs gradually improved between 2010 and 2016, pointing out improvements of level 1 SMOS TB products quality through the SMOS lifetime. The improvement shown from 2010 to 2014 relies on a consistent SMOS processor version and reanalysed ECMWF TBs of constant quality. So, it is entirely due to SMOS observations improvement, likely due to actions taken to manage RFI contamination. Improvements for 2015–2016 result from combined SMOS processor improvements and possible RFI contamination decrease. These results nevertheless clearly show an overall substantial quality improvement SMOS TB product at both polarisations between 2010 and 2014 and between 2015 and 2016.

The forward modelling results and bias correction results presented in this paper demonstrate the relevance of the SMOS observations for NWP applications. Long term monitoring results also open perspectives for SMOS and SMAP brightness temperatures data assimilation studies for environmental systems monitoring, prediction and long term reanalyses.

Declaration of competing interest

None

Acknowledgements

This work was partly funded under the ECMWF ESA-ESRIN contract number 4000101703/10/NL/FF/fk. The authors thank the reviewers for their constructive comments.

References

Albergel, C., Balsamo, G., de Rosnay, P., Muñoz-Sabater, J., Boussetta, S., 2012. A bare ground evaporation revision in the ECMWF land-surface scheme: evaluation of its impact using ground soil moisture and satellite microwave data. Hydrol. Earth Syst. Sci. 16, 3607–3620. https://doi.org/10.5194/hess-16-3607-2012.

Albergel, C., Dorigo, W., Reichle, R.H., Balsamo, G., de Rosnay, P., Muñoz-Sabater, J., Isaksen, L., de Jeu, R., Wagner, W., 2013. Skill and Global trend analysis of soil moisture from reanalyses and microwave remote sensing. J. Hydrometeorol. 14, 1259–1277. https://doi.org/10.1175/JHM-D-12-0161.1.

Albergel, C., Dutra, E., Bonan, B., Zheng, Y., Munier, S., Balsamo, G., de Rosnay, P., Muñoz-Sabater, J., Calvet, J.-C., 2019. Monitoring and forecasting the impact of the 2018 summer heatwave on vegetation. Remote Sens. 11 (5). https://doi.org/10.5194/hess-16-3607-2012.

Alfieri, L., Burek, P., Dutra, E., Krzeminski, B., Muraro, D., Thielen, J., Pappenberger, F., 2013. GloFAS global ensemble stream- flow forecasting and flood early warning. Hydrol. Earth Syst. Sci. 17, 1161–1175. https://doi.org/10.5194/hess-17-1161-2013.

Balsamo, G., Albergel, C., Beljaars, A., Boussetta, S., Cloke, H., Dee, D., Dutra, E., Muñoz-Sabater, J., Pappenberger, F., de Rosnay, P., Stockdale, T., Vitart, F., 2015. ERA-Interim/Land: a global land water resources dataset. Hydrol. Earth Syst. Sci. 19, 389–407. https://doi.org/10.5194/hess-19-389-2015.

Balsamo, G., Viterbo, P., Beljaars, A., van den Hurk, B., Hirsch, M., Betts, A., Scipal, K., 2009. A revised hydrology for the ECMWF model: verification from field site to terrestrial water storage and impact in the Itegrated Forecast System. J. Hydrometeorol. 10, 623–643.

Barbu, A., Calvet, J.-C., Lafont, S.a., 2014. Integrating ascat surface soil moisture and geov1 leaf area index into the surfex modelling platform: a land data assimilation application over France. Hydrol. Earth Syst. Sci. 18, 173–192.

Boussetta, S., Balsamo, G., Beljaars, A., Jarlan, L., 2013. Impact of a satellite-derived leaf area index monthly climatology in a global numerical weather prediction model. Int. J. Remote Sens. 34, 3520–3542.

Carrera, M., Bèlair, S., Bilodeau, B., 2015. The canadian land data assimilation system (caldas): description and synthetic evaluation study. J. Hydrometeorol. 16, 1293–1314. https://doi.org/10.1175/JHM-D-14-0089.1.

Carrera, M., Bélair, S., Bilodeau, B., Abrahamowicz, M., Alavi, N., Russell, A., Wang, X., 2017. Assimilation of SMAP brightness temperatures in environment and climate change Canada's new land surface parameterization scheme. In: 2017 IEEE International Geoscience and Remote Sensing Symposium (IGARSS), pp. 1589–1592.

Choudhury, B., Schmugge, T., Chang, A., Newton, R., 1979. Effect of surface roughness on the microwave emission from soils. J. Geophys. Res. 5699–5706.

Choudhury, B., Schmugge, T., Mo, T., 1982. A parameterization of effective soil temperature for microwave emission. J. Geophys. Res. 1301–1304.

Das, N., Entekhabi, D., Dunbar, R.S., Kim, S., Yueh, S., Colliander, A., O'Neill, P.E., Jackson, T., 2018. SMAP/Sentinel-1 L2 Radiometer/Radar 30-Second Scene 3 Km EASE-Grid Soil Moisture, Version 2. NASA National Snow and Ice Data Center Distributed Active Archive Center, Boulder, Colorado USA. https://doi.org/10.5067/KE1CSVXMI95Y.

De Lannoy, G., Reichle, R., 2015. Global assimilation of multiangle and multipolarization SMOS brightness temperature observations into the GEOS-5 catchment land surface model for soil moisture estimation. J. Hydrometeorol. 17, 669–691.

De Lannoy, G., Reichle, R., 2016. Assimilation of SMOS brightness temperatures or soil moisture retrievals into a land surface model. Hydrol. Earth Syst. Sci. 20, 4895–4911.

De Lannoy, G., Reichle, R., Pauwels, V., 2013. Global calibration of the GEOS-5 L-band

microwave radiative transfer model over nonfrozen land using SMOS observations. J. Hydrometeorol. 14, 765–785.
de Rosnay, P., Drusch, M., Boone, A., Balsamo, G., Decharme, B., Harris, P., Kerr, Y., Pellarin, T., Polcher, J., Wigneron, J.-P., 2009a. The AMMA land surface model intercomparison experiment coupled to the community microwave emission model (ALMIP-MEM). J. Geophys. Res. 114. https://doi.org/10.1029/2008JD010724.
de Rosnay, P., Drusch, M., Muñoz-Sabater, J., 2009b. SMOS Global Surface Emission Model. *ECMWF ESA Contract Report. ESA/ESRIN Contract Contract 20244/07/I-LG, MS1TN-Part1*.
de Rosnay, P., Drusch, M., Vasiljevic, D., Balsamo, G., Albergel, C., Isaksen, L., 2013. A simplified Extended Kalman Filter for the global operational soil moisture analysis at ECMWF. Q. J. R. Meteorol. Soc. 139, 1199–1213. https://doi.org/10.1002/qj.2023.
de Rosnay, P., Wigneron, J.-P., Holmes, T., Calvet, J.-C., Mätzler, C., Rosenkranz, P.W., Battaglia, A., Wigneron, J.P., 2006. Parameterizations of the effective temperature for L-band radiometry. Inter-comparison and long term validation with SMOSREX field experiment, Radiative Transfer Models for Microwave Radiometry. In: Matzler, Christian (Ed.), Thermal Microwave Radiation - Applications for Remote Sensing", IET Electromagnetic Waves Series 52, London, UK. Product Code: EW 052 0-86341-573-3 and 978-086341-573.
Dee, D., 2005. Bias and data assimilation. Q. J. R. Meteorol. Soc. 131, 3323–3343.
Dee, D., Uppala, S., Simmons, A., Berrisford, P., Poli, P., Kobayashi, S., Andrae, U., Balsameda, M., Balsamo, G., Bauer, P., Bechtold, P., Beljaars, A., van de Berg, L., Bidlot, J., Bormann, N., Delsol, C., Dragani, R., Fuentes, M., Geer, A., Haimberger, L., Healy, S., Hersbach, H., Hólm, E., Isaksen, L., Kållberg, P., Köhler, M., Marticardi, M., McNally, A., Monge-Sanz, B., Morcrette, J.-J., Park, B.-K., Peubey, C., de Rosnay, P., Tavolato, C., Thépaut, J.-N., Vitart, F., 2011. The ERA-Interim reanalysis: configuration and performance of the data assimilation system. Q. J. R. Meteorol. Soc. 137, 553–597. https://doi.org/10.1002/qj.828.
Dirmeyer, P.A., Gao, X., Guo, Z., Oki, T., Hanasaki, N., 2006. The Second Global Soil Wetness Project (GSWP-2): multi-model analysis and implications for our perception of the land surface. Bull. Americ. Met. Soc. 87 (10), 1381–1397.
Dobson, M., Ulaby, F., Hallikainen, M., EL-Rayes, M., 1985. Microwave dielectric behavior of wet soil-partii: dielectric mixing models. IEEE Trans Geosc. Sci 38, 1635–1643.
Documentation, I., 2018. Integrated forecasting system (IFS) documentation, physical processes. https://www.ecmwf.int/en/elibrary/18714-part-iv-physical-processes.
Draper, C., Reichle, R., De Lannoy, G., Liu, Q., 2012. Assimilation of passive and active microwave soil moisture retrievals. Geophys. Res. Lett. 39, L04401. https://doi.org/10.1029/2011GL050655.
Drusch, M., 2007. Initializing numerical weather prediction models with satellite-derived surface soil moisture: data assimilation experiments with ECMWFs Integrated Forecast System and the TMI soil moisture data set. J. Geophys. Res. 112, D03102. https://doi.org/10.1029/2006JD007478.
Drusch, M., Holmes, T., de Rosnay, P., Balsamo, G., 2009. Comparing ERA-40 based L-band brightness temperatures with Skylab observations: a calibration/validation study using the Community Microwave Emission Model. J. Hydrometeorol. https://doi.org/10.1175/2008JHM964.1. (in press).
Drusch, M., Wood, E., Gao, H., 2005. Observation operators for the direct assimilation of TRMM Microwave Imager retrieved soil moisture. Geophys. Res. Lett. 32, L19503. https://doi.org/10.1029/2005GL023623.
Dutra, E., Balsamo, G., Viterbo, P., Miranda, P., Beljaars, A., Schär, C., Elder, K., 2010. An improved snow scheme for the ecmwf land surface model: description and offline validation. J. Hydrometeorol. 11, 899–916. https://doi.org/10.1175/2010JHM1249.1.
Eagleman, J., Lin, W., 1976. Remote sensing of soil moisture by a 21-cm passive radiometer. J. Geophys. Res. 81, 3660–3666.
Entekhabi, D., Njoku, E., O'Neill, P., Kellog, K., Crow, W., Edelstein, W., Entin, J., Goodman, S., Jackson, T., Johnson, J., Kimball, J., Piepmeier, J., Koster, R., Martin, N., McDonald, K., Moghaddam, M., Moran, S., Reichle, R., Shi, J., Spencer, M., Thurman, S., Tsang, L., Van Zyl, J., 2010. The SoilMoistureActive passive (SMAP) mission. Proc. IEEE 98 (5), 704–716.
Escorihuela, M.-J., Kerr, Y.H., de Rosnay, P., Wigneron, J.-P., Calvet, J.-C., Lemaître, F., 2007. A simple model of the bare soil microwave emission at l-band. IEEE Trans. Geosci. Remote Sens. 45 (7), 1978–1987.
FAO, 2003. FAO digital soil map of the World (DSMW). In: Food and Agriculture Organization, Technical Report of the United Nations.
Fernandez-Moran, R., Al-Yaari, A., Mialon, A., Mahmoodi, A., Al Bitar, A., De Lannoy, G., Lopez-Baeza, E., Kerr, Y., Wigneron, J.-P., 2017. SMOS-IC: an alternative SMOS soil moisture and vegetation optical depth product. Remote Sens. 9. https://doi.org/10.3390/rs9050457.
Holmes, T., de Rosnay, P., de Jeu, R., Wigneron, J.-P., Kerr, Y.H., Calvet, J.-C., Escorihuela, M.-J., Saleh, K., Lemaître, F., 2006. A new parameterization of the effective temperature for L-band radiometry. Geophys. Res. Lett. 33, L07405. https://doi.org/10.1029/2006GL025724.
Holmes, T., Drusch, M., Wigneron, J.-P., de Jeu, R., 2008. A global simulation of microwave emission: error structures based on output from ECMWFs operational Integrated Forecast System. IEEE Trans. Geosci. Remote Sens. 46 (3), 846–856.
Jackson, T., O'Neill, P., 1990. Attenuation of soil microwave emission by corn and soybeans at 1.4and 5 ghz. IEEE Trans. Geosci. Remote Sens. 28 (5), 978–980.
Kerr, Y., Al-Yaari, A., Rodríguez-Fernández, N., Parrens, M., Molero, B., Leroux, D., Bircher, S., Mahmoodi, A., Mialon, A., Richaume, P., Delwart, S., Al Bitar, A., Pellarin, T., Bindlish, R., Jackson, T.J., Rüdiger, C., Waldteufel, P., Mecklenburg, S., Wigneron, J.-P., 2016. Overview of SMOS performance in terms of global soil moisture monitoring after six years in operation. Remote Sens. Environ. 180, 40–63.
Kerr, Y., Waldteufel, P., Richaume, P., Davenport, I., Ferrazzoli, P., Wigneron, J.-P., 2010a. Algorithm Theoretical Based Document (ATBD) for the SMOS Level 2 Soil Moisture Processor Development Continuation. SO-TN-ARR-L2PP-0037. issue 3.4.
Kerr, Y.H., Waldteufel, P., Richaume, P., Wigneron, J.-P., Ferrazzoli, P., Mahmoodi, A., Al Bitar, A., Cabot, F., Gruhier, C., Juglea, S., Leroux, D., A, M., Delwart, S., 2012. The SMOS soil moisture retrieval algorithm. IEEE Trans. Geosci. Remote Sens. 50, 1384–1403.
Kerr, Y.H., Waldteufel, P., Wigneron, J.-P., Cabot, F., Boutin, J., Escorihuela, M., Font, J., Reul, N., Gruhier, C., Juglea, S., Delwart, S., Drinkwater, M., Hahne, A., Martin-Neira, M., Mecklenburg, S., 2010b. The SMOS mission: new tool for monitoring key elements of the global water cycle. Proc. IEEE 98 (5), 666–687. https://doi.org/10.1109/JPROC.2010.2043032.
Kirdyashev, K., Chukhlantsev, A., Shutko, A., 1979. Microwave radiation of the earths surface in the presence of vegetation cover. Radiotekhnika Elektron. 24, 256–264.
Koster, R.D., Dirmeyer, P., Guo, Z., Bonan, G., Cox, P., Gordon, C., Kanae, S., Kowalczyk, E., Lawrence, D., Liu, P., Lu, C., Malyshev, S., McAvaney, B., Mitchell, K., Mocko, D., Oki, T., Oleson, K., Pitman, A., Sud, Y., Taylor, C., Verseghy, D., Vasic, R., Xue, Y., Yamada, T., 2004. Regions of strong coupling between soil moisture and precipitation. Sciences 305, 1138–1140.
Koster, R., Mahanama, P., Yamada, T., Balsamo, G., Berg, A., Boisserie, M., Dirmeyer, P., Doblas-Reyes, F., Drewitt, G., Gordon, C., Guo, Z., Jeong, J., Lee, W., Li, Z., Luo, L., Malyshev, S., Merryfield, W., Seneviratne, S., Stanelle, T., van den Hurk, B., Vitart, F., Wood, E., 2011. The second phase of the global land-atmosphere coupling experiment: soil moisture contributions to subseasonal forecast skill. J. Hydrometeorol. 12, 805–822.
Kumar, S., Peters-Lidard, C.,D., Mocko, D., Reichle, R., Liu, Y., Arsenault, K.R., Xia, Y., Ek, M., Riggs, G., Livneh, B., Cosh, M., 2014. Assimilation of remotely sensed soil moisture and snow depth retrievals fo drought estimation. J. Hydrometeorol. 15, 2446–2469.
Lawrence, H., Wigneron, J.-P., Demontoux, F., Mialon, A., Kerr, Y., 2013. Evaluating the semiempirical H?Q model used to calculate the L-band emissivity of a rough bare soil. IEEE Trans. Geosci. Remote Sens. 51 (7), 4075–4084.
Lievens, H., Al Bitar, A., Verhoest, N., Cabot, F., De Lannoy, G., Drusch, M., Dumedah, G., Hendricks Franssen, H., Kerr, Y., Tomer, S., Martens, B., Merlin, O., Pan, M., van den Berg, M., Vereecken, H., Walker, J., Wood, E., Pauwels, V., 2015. Optimization of a radiative transfer forward operator for simulating SMOS brightness temperatures over the upper Mississippi basin. J. Hydrometeorol. 16, 1109–1134.
Loveland, T., Reed, B., Brown, J., D.O., O., Zhu, Z., Youing, L., Merchant, J., 2000. Development of a global land cover characteristics database and igb6cover from the 1km avhrr data. Int. J. Remote Sens. 21, 1303–1330.
Mecklenburg, S., Drusch, M., Kaleschke, L., Rodríguez-Fernández, N., Reul, N., Kerr, Y., Font, J., Martin-Neira, M., Oliva, R., Daganzo-Eusebio, E., Grant, J., Sabia, R., Macelloni, G., Rautiainen, K., Fauste, J., de Rosnay, P., Muñoz-Sabater, J., Verhoest, N., Lievens, H., Delwart, S., Crapolicchio, R., de la Fuente, A., Kornbe, M., 2016. ESA's Soil Moisture and Ocean Salinity mission: from science to operational applications. Remote Sens. Environ. 180, 3–18. https://doi.org/10.1016/j.rse.2015.12.025.
Mialon, A., Wigneron, J.-P., de Rosnay, P., Escorihuela, M., Ker, Y., 2012. Evaluation the L-MEB model from long-term microwave measurements over a rough field, SMOSREX 2006. IEEE Trans. Geosci. Remote Sens. 50 (5), 1458–1467.
Mironov, V., Dobson, M., Kaupp, V., Komarov, S., Kleshchenko, V., 2004. Generalized refractive Mixing dielectric model for moist soils. IEEE Trans. Geosci. Remote Sens. 42 (4), 773–785.
Muñoz-Sabater, J., de Rosnay, P., Albergel, C., Isaksen, L., 2018. Sensitivity of soil moisture analyses to contrasting background and observation error scenarios. Water 10 (7).
Muñoz-Sabater, J., de Rosnay, P., Balsamo, G., 2011a. Sensitivity of L-band NWP forward modelling to soil roughness. Int. J. Remote Sens. https://doi.org/10.1080/01431161.2010.507260.
Muñoz-Sabater, J., de Rosnay, P., Jiménez, C., Isaksen, L., Albergel, C., 2014. SMOS brightness temperatures angular noise: characterization, filtering and validation. IEEE Trans. Geosci. Remote Sens. 52 (9), 5827–5839.
Muñoz-Sabater, J., Fouilloux, A., de Rosnay, P., 2011b. Technical implementation of SMOS data in the ECMWF integrated forecasting system. IEEE Trans. Geosci. Remote Sens. https://doi.org/10.1109/LGRS.2011.2164777.
Muñoz-Sabater, J., Lawrence, H., Albergel, C., de Rosnay, P., Isaksen, L., Drusch, M., Kerr, Y., Mecklenburg, S., 2019. Assimilation of SMOS brightness temperature in the ECMWF integrated forecasting system. Q. J. R. Meteorol. Soc. https://doi.org/10.1002/qj.3577.
Muñoz-Sabater, J., Rodríguez-Fernández, N., Richaume, P., Albergel, C., de Rosnay, P., Kerr, Y., 2016. SMOS Near-Real-Time Soil Moisture Processor: Operational Chain and Evaluation . ECMWF ESA Contract Report. ESA Contract 4000101703/10/NL/FF/fk, TR2PIII-Wp4020.
Njoku, E.G., Jackson, T., Lakshmi, V., Chan, T., Nghiem, S., 2003. Soil moisture retrieval from AMSR-E. IEEE Trans. Geosci. Remote Sens. 41 (2), 215–229.
Pellarin, T., Wigneron, J.-P., Calvet, J.-C., Berger, M., Douville, H., Ferrazzoli, P., Kerr, Y.H., Lopez-Baeza, E., Pulliainen, J., Simmonds, L., Waldteufel, P., 2003. Two-year global simulation of L-band brightness temperature over land. IEEE Trans. Geosci. Remote Sens. 41 (4), 2135–2139.
Pulliainen, J., Hallikainen, M., Grandell, J., 1999. HUT snow emission model and its applicability to snow water equivalent retrieval. IEEE Trans. Geosci. Remote Sens. 37, 1378–1390.
Reichle, R.H., De Lannoy, G., Forman, B., Liu, Q., Mahanama, S., Toure, A., 2011. Assessment and enhancement of MERRA land surface hydrology estimates. J. Clim. 24, 6322–6338.
Reichle, R.H., De Lannoy, G., Lui, Q., Ardizzone, J., Chen, F., Colliander, A., Conaty, A., Crow, W., Jackson, T., Kimball, J., Koster, R., Smith, E.B., 2016. Soil Moisture Active

Passive Mission L4_SM Data Product Assessment (Version 2 Validated Release), NASA GMAO Office Note, No. 12 (Version 1.0).
Reichle, R.H., Koster, R.D., 2004. Bias reduction in short reccords of satellite soil moisture. Geophys. Res. Lett. 31.
Richards, L.A., 1931. Capillary conduction of liquids in porous medium. Physics 1.
Rodríguez-Fernández, N., Muñoz-Sabater, J., Richaume, P., de Rosnay, P., Kerr, Y., Albergel, C., Drusch, M., Mecklenburg, S., 2017. SMOS near-real-time soil moisture product: processor overview and first validation results. Hydrol. Earth Syst. Sci. 21, 5201–5216.
Rodríguez-Fernández, N., Richaume, P., Muñoz Sbater, J., de Rosnay, P., Kerr, Y., 2016. SMOS Near-Real-Time Soil Moisture Processor: Recommended Neural Network Configuration and Algorithm Description. ECMWF ESA Contract Report. ESA/ESRIN Contract 4000101703/10/NL/FF/fk, WP4020 SO-TN-CB-GS-0049.
Scipal, K., Drusch, M., Wagner, W., 2008. Assimilation of a ers scatterometer derived soil moisture index in the ecmwf numerical weather prediction system. Adv. Water Resour. https://doi.org/10.1016/j.advwatres.2008.04.013.
Taylor, C., Clark, D., 2001. The diurnal cycle and African easterly waves: a land surface perspective. Q. J. R. Meteorol. Soc. 127, 845–867.
Taylor, C., de Jeu, R., Guichard, F., P, H., Dorigo, W., 2012. Afternoon rain more likely over dry soils. Nature 489, 423–426. https://doi.org/10.1038/nature11377.
Trenberth, K., Smith, L., Qian, T., Dai, A., Fasullo, J., 2007. Estimates of the global water budget and its annual cycle using observational and model data. J. Hydrometeorol. 8, 758–769.
Ulaby, F., Moore, R., Fung, A., 1986. In: Microwave Remote Sensing: Active and Passive, Vol III, from Theory to Application. Artech House, Dedham, MA.
van den Hurk, B., Viterbo, P., Beljaars, A., Betts, A., 2000. Offline Validation of the ERA40 Surface Scheme. ECMWF Technical Memorandum, pp. 295.
Viterbo, P., Beljaars, A.C.M., 1995. An Improved Land Surface Parameterization Scheme in the ECMWF Model and its Validation, vol. 75 ECMWF Technical report.
Wagner, W., Hahn, S., Kidd, R., Melzer, T., Bartalis, Z., Hasenauer, S., Figa-Saldaña, J., de Rosnay, P., Jann, A., Scheiner, S., Komma, J., Kubu, G., Brugger, K., Aubrecht, C., Züger, J., Gangkofner, U., Kienberger, S., Brocca, L., Wang, Y., Blöschl, G., Eitzinger, J., Steinnocher, K., Zeil, P., Rubel, F., 2013. The ascat soil moisture product: a review of its specifications, validation results, and emerging applications. Meteorol. Z. 22 (1), 5–33. https://doi.org/10.1127/0941-2948/2013/0399.
Wanders, N., Karssenberg, D., de Roo, A., de Jong, S., Bierkens, M., 2014. The suitability of remotely sensed soil moisture for improving operational flood forecasting. Hydrol. Earth Syst. Sci. 18, 2343–2357. https://doi.org/10.5194/hess-18-2343-2014.
Wang, J.R., Choudhury, B., 1981. Remote sensing of soil moisture content over bare field at 1.4 ghz frequency. J. Geophys. Res. 86, 5277–5282.
Wang, J.R., Schmugge, T., 1980. An empirical model for the complex dielectric permittivity of soils as a function of water content. IEEE Trans. Geosci. Remote Sens. 18, 288–295.
Wegmüller, U., Mätzler, C., 1999. Rough bare soil reflectivity model. IEEE Trans. Geosci. Electron. 37, 1391–1395.
Wegmüller, U., Mätzler, C., Njoku, E., 1995. Canopy opacity models. In: Passive Microwave Remote Sensing of Land-Atmosphere Interactions. VSP, Utrecht, The Netherlands, pp. 375.
Wigneron, J.-P., Jackson, T., O'Neill, P., De Lannoy, G., de Rosnay, P., Walker, J., Ferrazzoli, P., Mironov, V., Bircher, S., Grant, J., Kurum, M., Schwank, M., Muñoz-Sabater, J., Das, N., Royer, A., Al-Yaari, A., Al Bitar, A., Fernandez-Moran, R., Lawrence, H., Mialon, A., Parrens, M., Richaume, P., Delwart, S., Kerr, Y., 2017. Modelling the passive microwave signature from land surfaces: a review of recent results and application to the L-band SMOS and SMAP soil moisture retrieval algorithms. Remote Sens. Environ. 192, 238–272. https://doi.org/10.1016/j.rse.2017.01.024.
Wigneron, J.-P., Kerr, Y.H., Waldteufel, P., Saleh, K., Escorihuela, M.-J., Richaume, P., Ferrazzoli, P., de Rosnay, P., Gurney, R., Calvet, J.-C., Guglielmetti, M., Hornbuckle, B., Mätzler, C., Pellarin, T., Schwank, M., 2007. L-band Microwave Emission of the Biosphere (L-MEB) Model: description and calibration against experimental data sets over crop fields. Remote Sens. Environ. 107, 639–655.
Wigneron, J.-P., Laguerre, L., Kerr, Y.H., 2001. A simple parmeterization of the L-band microwave emission from rough agricultural soils. IEEE Trans. Geosci. Remote Sens. 39, 1697–1707.
Wilker, H., Drusch, M., Seuffert, G., Simmer, C., 2006. Effects of the near-surface soil moisture profile on the assimilation of L-band microwave brightness temperature. J. Hydrometeorol. 7, 433–442.
Yilmaz, T., Crow, W., 2013. The optimality of potential rescaling approaches in land data assimilation. J. Hydrometeorol. 14, 650–660.
Zhan, X., Zheng, W., Fang, L., Liu, J., Hain, C., Yin, J., Ek, M., 2016. A preliminary assessment of the impact of SMAP Soil Moisture on numerical weather Forecasts from GFS and NUWRF models. In: IEEE International Geoscience and Remote Sensing Symposium (IGARSS). vol. 2016. pp. 5229–5232.